

## AVERAGE SPECTRA OF MASSIVE GALAXIES IN THE SDSS

DANIEL J. EISENSTEIN<sup>1,2,16,17</sup>, DAVID W. HOGG<sup>3,4</sup>, MASATAKA FUKUGITA<sup>5</sup>, OSAMU NAKAMURA<sup>5</sup>,  
 MARIANGELA BERNARDI<sup>6,2,7</sup>, DOUGLAS P. FINKBEINER<sup>8</sup>, DAVID J. SCHLEGEL<sup>8</sup>, J. BRINKMANN<sup>9</sup>,  
 ANDREW J. CONNOLLY<sup>10</sup>, ISTVÁN CSABAI<sup>11,12</sup>, JAMES E. GUNN<sup>8</sup>, ŽELJKO IVEZIĆ<sup>8</sup>, DON Q. LAMB<sup>2</sup>,  
 JON LOVEDAY<sup>13</sup>, JEFFREY A. MUNN<sup>14</sup>, ROBERT C. NICHOL<sup>6</sup>, DONALD P. SCHNEIDER<sup>15</sup>,  
 MICHAEL A. STRAUSS<sup>8</sup>, ALEX SZALAY<sup>12</sup>, DON G. YORK<sup>2</sup>  
*Submitted to The Astrophysical Journal 8/18/2002*

### ABSTRACT

We combine Sloan Digital Sky Survey spectra of 22,000 luminous, red, bulge-dominated galaxies to get high  $S/N$  average spectra in the rest-frame optical and ultraviolet (2600 Å to 7000 Å). The average spectra of these massive, quiescent galaxies are early-type with weak emission lines and with absorption lines indicating an apparent excess of  $\alpha$  elements over solar abundance ratios. We make average spectra of subsamples selected by luminosity, environment and redshift. The average spectra are remarkable in their similarity. What variations do exist in the average spectra as a function of luminosity and environment are found to form a nearly one-parameter family in spectrum space. We present a high signal-to-noise ratio spectrum of the variation. We measure the properties of the variation with a modified version of the Lick index system and compare to model spectra from stellar population syntheses. The variation may be a combination of age and chemical abundance differences, but the conservative conclusion is that the quality of the data considerably exceeds the current state of the models.

*Subject headings:* cosmology: observations — galaxies: abundances — galaxies: clusters: general — galaxies: elliptical and lenticular, cD — galaxies: evolution — methods: statistical

### 1. INTRODUCTION

Luminous elliptical and bulge-dominated galaxies are the most massive galaxies in the Universe. These objects show little rotation, have smooth radial profiles, are massive and kinematically hot, have a narrow range of stellar-mass-to-light ratios, show high metallicities, and reside preferentially in the Universe's denser environments (e.g., Kormendy & Djorgovski 1989; Roberts & Haynes 1994; Bender & Saglia 1999). These galaxies are also the most

intrinsically luminous galaxies in the Universe (e.g., Tammann et al. 1979; Blanton et al. 2001a). That the most optically luminous galaxies are red is remarkable, given that unextincted red stellar populations generally have higher stellar mass than blue populations at constant luminosity; it means that they are considerably more massive than their bluer, fainter spiral neighbors.

A common paradigm for the formation of bulge-dominated systems is hierarchical merging of smaller, star-forming progenitors (Barnes & Hernquist 1992; Kauffmann 1996; Baugh et al. 1996). In this model, the systems appear old and metal-rich because the merging is more common at high redshift and because the resulting starburst consumes or expels the remaining gas, thereby ending star formation (Kauffmann & Charlot 1998). This dependence upon cosmological merger rates and feedback suggests that the stellar populations of bulges should display subtle but important dependencies on mass and environment.

In this paper, we study the aggregate stellar populations of luminous, red, bulge-dominated galaxies using averaged spectra from the Sloan Digital Sky Survey (SDSS; York et al 2000). We select these galaxies because we know that they dominate the stellar mass density of the Universe (Fukugita et al. 1998; Hogg et al. 2002) and because they show great regularities in their properties (e.g., Faber 1973; Visvanathan & Sandage 1977; Djorgovski & Davis 1987; Dressler et al. 1987; Kormendy & Djorgovski 1989; Bower et al. 1992; Roberts & Haynes 1994; Bernardi et al. 2001). In addition, the great age of their stellar populations ease some, but not all, of the difficulties in understanding superimposed younger populations (Faber 1972; O'Connell 1976; Gunn et al. 1981; Charlot et al. 1996).

As the luminosity-weighted average spectrum does measure the total stellar population of an entire sample of galaxies, it is a well-defined mean property that can be compared to theoretical models of galaxy formation (Baldry et al. 2002, e.g.). We focus not on the interpretations

<sup>1</sup> Steward Observatory, University of Arizona, 933 N. Cherry Ave., Tucson, AZ 85121

<sup>2</sup> University of Chicago, Astronomy & Astrophysics Center, 5640 S. Ellis Ave., Chicago, IL 60637

<sup>3</sup> Center for Cosmology and Particle Physics, Department of Physics, New York University, 4 Washington Place, New York, NY 10003

<sup>4</sup> Institute for Advanced Study, Princeton, NJ 08540

<sup>5</sup> Institute for Cosmic Ray Research, University of Tokyo, Kashiwa, 2778582, Japan

<sup>6</sup> Department of Physics, Carnegie Mellon University, Pittsburgh, PA 15213

<sup>7</sup> Fermilab National Accelerator Laboratory, P.O. Box 500, Batavia, IL 60510

<sup>8</sup> Princeton University Observatory, Peyton Hall, Princeton, NJ 08544

<sup>9</sup> Apache Point Observatory, P.O. Box 59, Sunspot, NM 88349

<sup>10</sup> University of Pittsburgh, Pittsburgh, PA

<sup>11</sup> Department of Physics of Complex Systems, Eötvös University, Pázmány Péter sétány 1, H-1518 Budapest, Hungary

<sup>12</sup> Department of Physics and Astronomy, The Johns Hopkins University, 3701 San Martin Drive, Baltimore, MD 21218

<sup>13</sup> Astronomy Centre, University of Sussex, Falmer, Brighton BN1 9QJ, UK

<sup>14</sup> United States Naval Observatory, Flagstaff Station, P.O. Box 1149, Flagstaff, AZ 86002

<sup>15</sup> Department of Astronomy and Astrophysics, Pennsylvania State University, University Park, PA 16802

<sup>16</sup> Hubble Fellow

<sup>17</sup> Alfred P. Sloan Fellow

of the average spectrum itself, but rather on the variations of this average with luminosity, environment, and redshift. These variations should be able to test predictions that more luminous (or massive) galaxies have higher metallicity and galaxies in clusters have older stellar populations. Previous observational studies (e.g., Bower et al. 1990; Guzman et al. 1991; Rose et al. 1994; James & Mobasher 1999; Terlevich et al. 1999; Poggianti et al. 2001) comparing spectra of individual galaxies have found evidence to support these hypotheses. Of course, one would also expect to find that galaxies at high redshift should have younger stellar populations than similar galaxies at low redshift, but even this trend can be altered if massive, bulge-dominated galaxies are still forming at low redshift (Franx 1995; van Dokkum & Franx 2001).

Because we are interested in comparing the average spectra of samples, it is critical that the samples be selected so that the variation between the samples is as controlled as possible. With SDSS data, we can select uniform samples according to rest-frame photometry and morphological properties across a wide range of environments and redshifts, allowing trends in the data to be attributed to astrophysics rather than selection biases.

The average spectra are of extremely high signal-to-noise ratio, thereby allowing analyses that would be impractical on individual SDSS spectra. Over 100 absorption lines are apparent in the composite. Indeed, the resulting spectra exceed the ability of the best spectral models of stellar populations to interpret, especially given the non-solar ratio of  $\alpha$ -element to iron-peak abundances (Worthey et al. 1992; González 1993; Davies et al. 1993; Paquet 1994; Worthey 1998; Proctor & Sansom 2002) apparent in the data.

The outline of this paper is as follows. In § 2, we describe the relevant aspects of SDSS data and introduce the methods for our analysis, including principal component analysis (PCA) and a modification of the Lick absorption line index system. In § 3, we describe our sample selection and environment estimation. We present a general analysis of the average spectra in § 4 and analysis of the variations with luminosity and environment in § 5. Variations with redshift are presented in § 6. In § 7, we use the highest redshift sample to determine the average spectrum in the mid-ultraviolet. We conclude in § 8.

Except where noted otherwise, we adopt a conventional cosmological world model with  $H_0 = 100 h \text{ km s}^{-1} \text{ Mpc}^{-1}$  and  $(\Omega_M, \Omega_\Lambda) = (1/3, 2/3)$ .

## 2. DATA AND PROCEDURES

### 2.1. SDSS Imaging

The SDSS is obtaining  $u$ ,  $g$ ,  $r$ ,  $i$  and  $z$ -band drift-scan images of the Northern Galactic Cap and spectra of roughly  $10^6$  galaxies in that region (York et al 2000). The photometric system and imaging hardware are described in detail elsewhere (Fukugita et al. 1998; Gunn et al. 1998; Hogg et al. 2001; Smith, Tucker et al. 2002). An automated image-processing system detects astronomical sources and measures photometric and astrometric properties (Lupton et al. 2001; Stoughton et al. 2002; Pier et al. 2002; Lupton et al. 2002) of them. Finally, galaxies are selected for spectroscopy by two algorithms (Strauss et al. 2002; Eisenstein et al. 2001) described further in § 3.

The photometric parameters of interest for this study are as follows. The Petrosian (1976) radius  $\theta_{r,\text{pet}}$  is the angular radius at which the mean surface brightness of the source in the SDSS  $r$ -band image inside that radius is five times higher than the mean surface brightness in a narrow annulus centered on that radius. The Petrosian flux (with corresponding magnitude  $m_{\text{pet}}$ ) is the total flux (in any of the five SDSS bandpass images) within a circular aperture of radius  $2\theta_{r,\text{pet}}$  (twice the Petrosian radius in the  $r$ -band). The half-light and 90% radii  $\theta_{50}$  and  $\theta_{90}$  are the angular radii within which 50% and 90% of the  $r$ -band Petrosian flux is found. The concentration  $c$  is defined to be the ratio  $\theta_{90}/\theta_{50}$ . The de Vaucouleurs likelihood  $L_{\text{dev}}$  is the likelihood that the galaxy's  $r$ -band 2-dimensional image was generated by a true de Vaucouleurs elliptical profile convolved with the seeing. The exponential likelihood  $L_{\text{exp}}$  is a similar likelihood of an exponential profile. The model magnitude  $m_{\text{model}}$  is the total magnitude corresponding to the best-fit profile, which is the best-fit de Vaucouleurs profile for all galaxies in this study. All magnitudes are corrected for extinction using the Schlegel et al. (1998) predictions.

Two samples of galaxies are selected from the SDSS imaging for spectroscopy. The larger sample, with about 88% of the allotment, is a flux-limited sample of galaxies that extends to  $r_{\text{Petro}} < 17.77$  (Strauss et al. 2002). We refer to this as the MAIN sample. The smaller portion, with the remaining 12% of the allotment, uses two color-magnitude cuts to seek luminous, early-type galaxies that are fainter than the MAIN limit. This sample is known as the luminous, red galaxy (LRG) sample. The LRG sample is roughly volume-limited to  $z \approx 0.4$  and contains additional galaxies to  $z \approx 0.55$  with a flux limit of  $r_{\text{Petro}} = 19.5$ . Further details are found in Eisenstein et al. (2001).

### 2.2. SDSS Spectroscopy

The SDSS uses two fiber-fed double-spectrographs to measure spectra of objects from 3800 Å to 9200 Å with a resolution of about 1800. Each plug plate holds 640 fibers, yielding 608 spectra of galaxies, quasars, and stars and 32 sky spectra per pointing (Blanton et al. 2001b). Fibers cover 3'' diameter circular apertures on the sky. Each spectrograph handles 320 fibers (which we call a half-plate), and the two halves are reduced independently.

In detail, the instrumental resolution and pixel scale are close to constant in logarithmic wavelength rather than wavelength. The instrumental resolution is about  $170 \text{ km s}^{-1}$  FWHM. The `id1Spec2d` software pipeline (Schlegel, Burles, et al., in prep) combines multiple exposures of a given object and resamples the total spectrum onto a grid of wavelengths that is logarithmically-spaced by  $69.1 \text{ km s}^{-1}$ .

The flux calibration procedure is summarized in Stoughton et al. (2002, § 3.3 & 4.10.1) and will be fully detailed in Schlegel, Burles, et al. (in prep). The flux calibration is imposed on each plate by a set of 8 spectrophotometric standard stars, chosen by color to be F subdwarf stars. The SDSS does not use an atmospheric refraction corrector, so the effective fiber position on the sky shifts slightly as a function of wavelength. In the presence of brightness gradients, this creates a fluxing error. This is corrected by referring the broadband spectrophotometry to  $5'' \times 8''$

aperture “smear” exposures. As early-type galaxies have small color gradients, we expect that this smear correction will remove the effects of atmospheric refraction.

The spectrophotometric calibration appears to be correct in the average to better than 10%. Since each average spectrum involves galaxies from a moderate range of redshifts, systematic wavelength-dependent spectrophotometry biases in the average spectra will be strongly suppressed on scales below a few hundred Å. Comparing our average spectra in different redshift bins (see § 3.2) shows differences of under 10% (4% *rms*), some of which may be due to actual evolution. As this involves comparison of spectrophotometry at different observed wavelengths, we infer that the mean spectrophotometry is accurate at this level, up to perhaps an overall tilt. We will return to this point in § 5.2. Recent efforts (Tremonti & Schlegel, private communication) suggest that the current calibrations are slightly too blue (roughly 10% in flux over the spectral range) with additional residuals blueward of 4300 Å (observed frame).

Redshifts are found by comparing to stellar templates (Frieman et al., in prep.; Schlegel et al., in prep.). Repeat observations show that the errors in the redshift estimates are less than 30 km s<sup>-1</sup> for MAIN sample galaxies and degrade to about 100 km s<sup>-1</sup> for the highest redshift LRGs.

### 2.3. Spectroscopic Sample

We use spectra from 261 separate plates; a total sample of about 120,000 galaxies. Certain plates have been observed more than once, and a small fraction of objects appear on more than one plate (for quality assurance). We use only one spectrum of each object, chosen by the best median signal-to-noise ratio on each candidate half-plate. Only plates that meet survey quality standards are used.

A few spectra were found to contain sufficiently serious reduction failures as to dominate the principal component analysis; we rejected the entire plate in this case (so as not to skew the average by some undetected pattern among the corrupted objects). This eliminated 12 plates, although some of these had other exposures that could have been used.

We select samples of red, bulge-dominated galaxies from these plates; the selection is described in § 3.

### 2.4. Principal component analysis

We are interested in average spectra; however, we choose to go further and perform principal component analyses (PCA) on each set of spectra. This isolates a set of eigenspectra ranked by the amount of the total variance in the input set that each explains. PCA is useful for identifying variations in the spectra beyond the mean, and we find that emission line components are isolated by this technique.

We can recover the average spectra from the PCA decomposition by finding the mean of each PCA coefficient and summing the eigenspectra weighted by these means. Were we to include all the eigenspectra, the resulting linear combination would be exactly the average of the spectra used as input to the PCA. However, we include only the first 20 eigenspectra. We have verified that this procedure makes no difference relative to the true average; the means

of the PCA coefficients converge rapidly to zero. One can see that the truncation does not constitute a smoothing of the spectra by noting that permuting the order of the pixels within the definition of the spectral space would not affect the PCA results.

We begin with spectra in  $F_\lambda$  units, but we use the redshifts to rescale each source to its intrinsic luminosity spectrum  $L_\lambda$ . This does not fully reproduce the mean spectrum of a volume-limited set of galaxies, but in practice the luminosity range of our samples are sufficiently narrow—0.5 mag—that the corrections to a volume-limited mean are negligible. To close approximation, each average spectrum will represent the volume-averaged stellar population of galaxies with the chosen intrinsic properties.

Before performing the PCA step, we pre-condition the spectra. We shift each spectrum to the rest frame according to its redshift. We do not include shifts smaller than a unit spacing of our wavelength grid (69.1 km s<sup>-1</sup>). This is equivalent to adding a small additional velocity dispersion to the sample; however, the effect is only 20 km s<sup>-1</sup> ( $69 \div \sqrt{12}$ , the standard deviation of a boxcar), which is small compared to the actual velocity dispersions of the galaxies. We then select a particular range of rest-frame wavelengths, say 3650 Å to 7000 Å, to ensure that the full range of wavelengths is covered by SDSS spectra for the full range of redshifts included in a particular sample.

We iteratively interpolate over pixels for which `id1Spec2d` has set warning mask flags. We begin by linear interpolating over all masked pixels and computing the mean spectrum. We then return to the masked pixels, interpolate with the mean spectrum times a linear function, and recompute the mean. We repeat this step four times to ensure convergence. We increase the masked region around the sky features at 5577 Å, 5890 Å, 5896 Å, 6300 Å, 6364 Å, 7245 Å, and 7283 Å, typically to 10 Å, so as to avoid rare problems of poor sky subtraction. Since the samples involve a wide range of redshift, masking at a fixed observed wavelength enters at different rest-frame wavelengths and therefore has little effect on the average spectrum. We remove entirely any objects that have more than 20 pixels masked for missing data (not counting pixels in the first and last 50 pixels of a given spectrum).

We subtract the continuum of each individual spectrum by removing the first  $N_F$  sinusoidal components. We pick  $N_F = 8$  for our 3650 Å to 7000 Å stacking,  $N_F = 6$  for 3500 Å to 6000 Å stacking, and  $N_F = 5$  for 2600 Å to 4400 Å stacking. We have tried other choices with little change. For example, we have tried extracting narrow wavelength regions with no continuum subtraction and get the same answers.

Because we subtract the continuum from our spectra before performing the PCA, our eigenspectra lack a continuum. We restore this continuum after the PCA step by adding back the average of the subtracted continua. This procedure exactly reproduces the mean spectrum but protects the PCA from being dominated by broad-band variations. When comparing spectra from different samples, we rescale to a common overall amplitude but do not otherwise adjust the continua.

Before performing the PCA, we renormalize the different wavelengths by the inverse of the average error in that pixel. This doesn’t affect the average spectrum but does

affect subsequent components. In practice, the weighting is mild. After performing the PCA, or more exactly, the diagonalization of the product of the matrix of spectra with its transpose, we restore the original physical normalization of the wavelengths in each eigenspectrum.

In practice, we find that a single component dominates the spectrum of eigenvalues. This eigenspectrum shows a familiar early-type absorption line spectrum. Because the ratio of this eigenvalue to the others is so large, the first component can deviate only slightly from the mean of the dataset.

Regarding different samples, it is important to stress that the entire PCA process has been applied to the two sets of galaxies completely independently. In particular, the comparison of average spectra is not constrained to differ only in a low (20) dimensional subspace of retained eigenspectra.

### 2.5. Error estimation

To construct an estimate of the error on the average spectrum, we divide each sample into two, find the average spectrum of each half, and analyze the rms differences between the two halves. Before differencing, we remove 20 low-pass sinusoidal modes (from over 2000 pixels) to be sure that the continuum is not affecting our estimate of the small-scale noise. There is essentially no structure apparent in the differenced spectra. Because there are small correlations between neighboring pixels (e.g. because of the sub-pixel wavelength shifts between exposures), we smooth the difference with a box car filter of 5 pixel width and multiply the result by  $\sqrt{5}$ . Were the pixels independent, this would not matter, but for correlated pixels this smoothing creates the residual that should apply to multi-pixel averages such as are found in spectral indices. We form the square of the smoothed difference spectrum and then smooth with a 100 pixel box-car. This effectively creates the variance of the differenced spectrum as a function of wavelength.

The galaxies are split into the two halves according to whether their plate number is even or odd. This means that reduction errors that might affect an entire plate are included in the noise estimate, because all of the affected galaxies will go into one half or the other. Conversely, any secular changes in target selection algorithm or imaging properties are isolated from the error analysis. If we had divided the sample into early plates and the late plates, small differences in target selection (perhaps simply caused by different photometric calibrations in different parts of the sky) could have resulted in artificial differences between the mean spectra.

If one has two spectra of equal signal-to-noise ratio, then the noise in the difference is twice the noise in the average. Hence, as our even and odd spectra should have quite similar signal-to-noise ratio, we estimate the variance in the average spectra as being one quarter of that in the smoothed square difference.

Although the noise in a single spectrum can be a complicated and spiky function of wavelength due to the presence of sky lines and detector flaws, the noise in the combined spectrum should be a smooth function of wavelength. Noise features at a narrow observed wavelength range are smeared out by the superposition of many different redshifts, while

detector issues such as bad CCD columns are eliminated by the superposition of spectra from many different positions in the detector. Only the broad variations in response across wavelength (e.g., the drop in sensitivity shortward of 4000Å) should survive to affect the noise in the stacked spectrum.

The error at certain rest-frame wavelengths is dominated not by photon noise but rather by the shot noise of the presence of rare galaxies in the sample. In particular, a small fraction of our selected galaxies have emission lines, and the presence or absence of a few strong emission-line galaxies can affect the results at the line wavelengths. We could treat this by bootstrap resampling of the input samples, but the line emissions are sufficiently weak that we will focus only on the isolation and subtraction of the lines and not on the error in that subtraction.

The signal-to-noise ratios of the average spectra are very high, typically a few hundred per pixel (see Table 1). Because our error estimation is based on internal differences, it does not account for errors that are common to the two half samples. Generally, systematic effects are functions of observed wavelength, which means that their impact will be smeared out by the combination of objects of different redshifts. This suppresses such error modes on scales less than a few hundred Å. We have few ways at present to assess the errors on larger scales, but the differencing of samples at very different redshifts do suggest that the errors are small (4% *rms*). We are not aware of any systematic effects that would be functions of rest-frame wavelength. We will present another validation of the quoted errors in § 5.2.

### 2.6. Comparison between spectra and to models

The galaxies in the samples to be defined in § 3 differ in their velocity dispersions. In order to make fair comparisons among the average spectra, we therefore smooth all the average spectra to a common velocity dispersion of  $\sigma_v = 325 \text{ km s}^{-1}$ , which is the largest velocity dispersion of the individual samples.

In order to interpret our average spectra in terms of age, metallicity, or other variations, we need to compare our spectra to model spectra of stellar population synthesis models. We use the models of Vazdekis (1999) (hereafter V99), who provides 2Å resolution spectra of single-age, single-metallicity, solar-element ratio stellar populations. Because the resolution of these models is better than the resolution achieved in galaxies with large velocity dispersion, we can treat these model spectra identically to our data and thereby do fair comparisons between the two. We use single power-law initial mass function V99 models throughout.

### 2.7. *sLick* indices

We measure absorption line strengths by a revision of the most recent version of the “Lick” system (Faber et al. 1985; Worthey et al. 1994; Trager et al. 1998). In addition to the standard Lick indices, we have included 4 indices for measuring the H $\gamma$  and H $\delta$  absorption lines (Worthey & Ottaviani 1997). The Lick system involves measuring line fluxes in narrow wavelength ranges relative to a “pseudo-continuum” found by linearly interpolating between two spectral averages on either side of the lines.

We cannot match the fluxing and calibration of the Lick system but have attempted an intermediate step of matching the wavelength-dependent resolution of the Lick IDS instrument (using a linear interpolation of the table in Worthey & Ottaviani 1997). The highest velocity dispersions of any of our spectra is  $325 \text{ km s}^{-1}$  at SDSS resolution. This corresponds to  $275 \text{ km s}^{-1}$  at  $6000\text{\AA}$  as smoothed to Lick IDS resolution. Hence, when computing indices, we smooth our spectra to match, at each wavelength, an intrinsic dispersion of  $275 \text{ km s}^{-1}$  at the Lick IDS resolution. For example, this corresponds to  $450 \text{ km s}^{-1}$  at  $4000\text{\AA}$ . The result is the spectrum of a galaxy with  $275 \text{ km s}^{-1}$  dispersion as it would be observed by the Lick IDS instrument. Because, strictly speaking, the Lick system is defined at zero velocity dispersion (at Lick IDS spectral resolution), we refer to the indices used in this work, normalized to  $275 \text{ km s}^{-1}$ , as smoothed-Lick or “sLick” indices.

We introduce the sLick indices rather than work on the true Lick system because (a) The Lick IDS spectra were referenced to a tungsten blackbody for overall calibration; (b) the indices are, strictly speaking, calibrated to a defined set of standard stars, which have not been observed with the SDSS telescope; and (c) the Lick system is defined at zero velocity dispersion, at which no galaxies can ever be observed, although some empirical corrections for velocity dispersion have been defined (Trager et al. 1998). For all these reasons, direct comparison of our sLick index measurements (in Table 2) to measurements in the Lick system found in the literature must be made with care.

On the other hand, we have treated the V99 model spectra in an identical way to the observed spectra, so the internal consistency of comparing our observed indices with the models is reliable. For the same reason, our measurements of differences or derivatives of sLick indices among our average spectra given in Table 2 are accurate.

### 3. MASSIVE GALAXY SAMPLES IN THE SDSS

#### 3.1. Morphology and color selection in the MAIN sample

The MAIN sample contains galaxies of all types, but we would like to select massive, red, bulge-dominated galaxies. We do this selection primarily on the basis of morphology but cannot avoid the need to remove color outliers.

We consider 4 luminosity bins within the MAIN sample of galaxies:  $-20.5 < M_r < -21$ ,  $-21 < M_r < -21.5$ ,  $-21.5 < M_r < -22$ , and  $-22 < M_r < -22.5$ . These absolute magnitudes are  $k + e$  corrected, de-reddened,  $r$ -band Petrosian magnitudes. We use the bandpass and evolution ( $k + e$ ) correction of a passively evolving old stellar population (Eisenstein et al. 2001) to adjust the galaxy photometry to  $z = 0$ . Since the redshift range of each bin is small and since the evolution correction is only 1 mag per unit redshift, the assumed evolution correction is not important for the results but merely serves to compare the galaxies to those at  $z = 0$ . Note that  $M_r^* \approx -20.8$  from the SDSS luminosity function (Blanton et al. 2001a), so the least luminous bin has galaxies whose luminosity is roughly  $L^*$ , while the most luminous bin has galaxies four times more luminous.

We make two purely morphological cuts on the sample: 1) we require that the inverse concentration  $1/c$  be less than 0.37, and 2) we require that the de Vaucouleurs

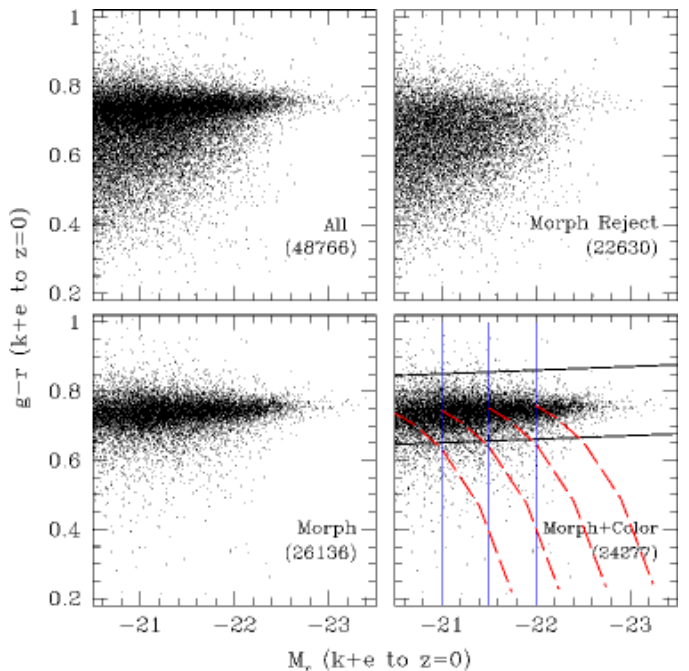


FIG. 1.— Rest-frame  $g-r$  color versus absolute  $r$ -band magnitude (both corrected for passive evolution) of MAIN galaxies. The effects of the morphological radial profile cuts is shown in the bottom two panels. Galaxies failing the morphology cut are in the upper right panel. The lower right panel shows the color cuts and luminosity bins. The dashed lines show the locus of color and magnitude of an old population with a fading 20% young single-age burst (Bruzual & Charlot 2001). We stress that the color cut is excluding many fewer galaxies at fixed stellar mass than at fixed luminosity.

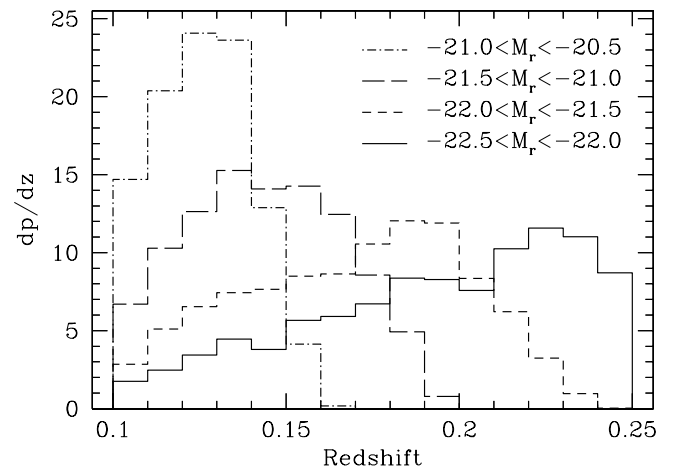


FIG. 2.— The redshift histograms for the MAIN galaxy luminosity-binned samples.

model fit be 20 times more likely than the exponential fit (excluding galaxies for which both likelihoods underflow to zero). See § 2.1 for the definitions of these statistics. Both of these cuts favor the traditional surface brightness profiles of elliptical galaxies and bulges. We do not perform cuts on the asymmetries or residual lumpiness of the galaxy.

We find that these radial profile cuts do significantly alter the distribution of galaxies in a rest-frame color versus absolute magnitude plot. The red sequence of early-type galaxies is strongly favored. Based on similar samples in



Shimasaku et al. (2002), Strateva et al. (2001), and Hogg et al. (2002), we expect that more than 2/3 of the sample are of E/S0 morphology, with the remainder being early-type spirals.

Figure 1 shows the distribution of galaxies in rest-frame color versus absolute magnitude with and without the morphological cuts. A small fraction of the radial-profile-selected galaxies lie well below the red sequence in  $g-r$ . If one considers slices at constant  $r$ -band luminosity, this fraction of blue galaxies is  $\sim 5\%$ . It should be stressed that the fraction of blue galaxies in slices of constant stellar mass would be considerably lower. Blue galaxies fade as they age and redden. Hence, one should compare the number of lower luminosity galaxies on the red sequence to the number of higher luminosity blue galaxies. In Figure 1, we display the loci of magnitude and color populated by a burst of 20% of new stars on top of an old population, using models from Bruzual & Charlot (2001). Following these curves rather than lines of constant luminosity, we would say that very few massive galaxies have been excluded by our color cut. In this model, 20% bursts require about 2 Gyr to redden enough to pass our color cut.

As we are interested in massive quiescent galaxies, we decide to cut these blue outliers using a color cut. We fit the rest-frame color-magnitude relation to a line of  $(g-r)_0 = 0.74 - 0.014(M_r + 20)$  and keep only those galaxies that fall within 0.1 mag in rest-frame color (region shown in Figure 1). This excludes 3% of the galaxies in the highest luminosity bin and 8% in the lowest (see Table 1).

Our color selection obviously excludes vigorously star-forming galaxies from the sample. Hence, we cannot claim that the average spectrum we find represents the average light from *all* bulge-dominated systems. The average age of the sample will be biased towards older ages (although of course the dominant problem in interpretation of optical spectra is the opposite, namely that a few young stars will bias the inferred age low).

We would prefer to compare galaxies at equal redshifts, and therefore we restrict our sample to redshifts between 0.1 and 0.25. However, our lower luminosity subsamples are drawn from a characteristically lower portion of this range, so there may be a small amount of passive evolution mixed into the spectral comparison across luminosity. Histograms of the redshift distribution are shown in Figure 2.

Table 1 lists the sample size, mean redshift, mean luminosity, selection properties, and average spectrum signal-to-noise ratio for the four luminosity samples (see the rows with environment “All”), as well as for the environment and redshift samples discussed in the next two sections.

### 3.2. Luminous LRG selection

Eisenstein et al. (2001) show that the LRG spectroscopic sample contains luminous galaxies with red rest-frame colors and early-type spectra out to  $z \approx 0.55$ . The sample is roughly volume-limited at  $z < 0.4$ ; however, the selection does create an oblique dependence on luminosity and rest-frame color. Intrinsically bluer galaxies must be more luminous than their redder cousins to enter the sample.

Luminous galaxies drawn from the MAIN sample at  $0.15 < z < 0.2$ , where there is no color selection, show

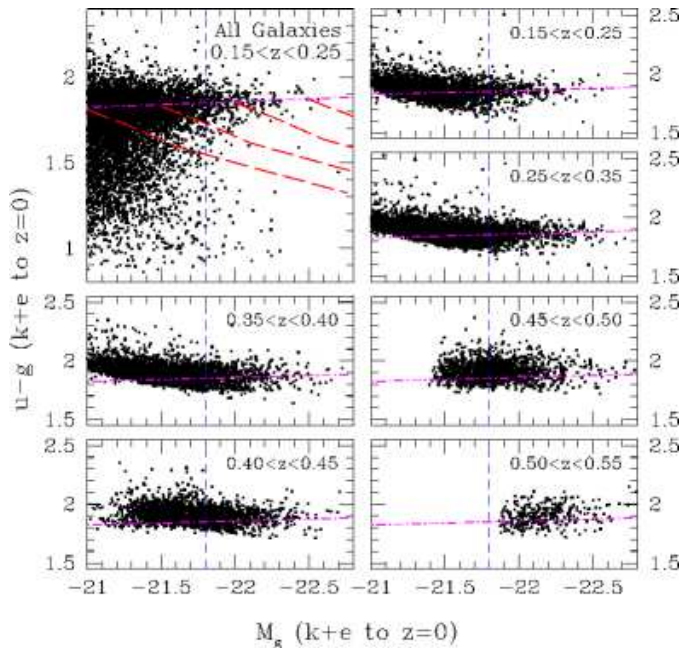


FIG. 3.— The rest-frame color versus magnitude (both corrected for passive evolution) distribution of (*upper left panel*) all galaxies at  $0.15 < z < 0.25$  and (*other panels*) LRGs in different redshift slices. The horizontal dot-dashed line is a fit to the color-magnitude locus of the red sequence. The full LRG sample would result in a bias towards galaxies on the red side of the red sequence. By imposing an additional magnitude cut (vertical dashed line), we can include the whole red sequence. The sample is volume-limited to  $z \approx 0.5$ . The diagonal dashed lines are fading bursts as in Figure 1.

an obvious ridge in color-magnitude space from the prevalence of early-type galaxies. At the highest luminosities, the red sequence is particularly obvious because the frequency of galaxies drops significantly blueward of the sequence. We would like to select all of the galaxies on the red sequence.

This red sequence is quite narrow, but not infinitely so. Hence, we have the problem that for some range of luminosities, galaxies on the red side of the red sequence would qualify for the LRG sample while those on the blue side would not. To gather a sample for which the entire red sequence will be included, we must use an even higher luminosity cut than the normal LRG selection criteria.

We therefore require  $M_g < -21.8$  within the LRG sample. This luminosity refers to the passively evolved, rest-frame  $g$ -band luminosity  $k$ -corrected from the  $r$ -band Petrosian magnitude, as described in Eisenstein et al. (2001). For comparison to our samples from MAIN, we note that this cut corresponds to  $M_r \lesssim -22.55$ . As shown in Figure 3, this cut allows the LRG sample to include the full red sequence. In addition, the higher luminosity cut means that the sample, which would otherwise be subject to flux limitations at  $z \gtrsim 0.40$ , retains its volume-limited nature until  $z \approx 0.5$ .

We limit the LRG selection to  $0.15 < z < 0.50$  and divide this into three redshift bins 0.1 in width plus a fourth bin at  $0.45 < z < 0.50$ . The limit at low redshift is primarily due to the small number of sufficiently luminous galaxies in the small closer volume. Similarly, there are not many galaxies in the LRG sample at  $z > 0.50$ , and these would not be volume-limited to  $M_g = -21.8$ .

TABLE 1

SUMMARY OF SAMPLE PROPERTIES								
Magnitude	Environment	Number	Used	S/N	$\langle z \rangle$	$\langle M_r \rangle$	$\sigma$ applied	Color reject
$-22.5 < M_r < -22.0$	All	2568	2394	487	0.193	-22.19	166	72
$-22.5 < M_r < -22.0$	$0 \leq N \leq 3$	356	326	159	0.197	-22.17	170	21
$-22.5 < M_r < -22.0$	$4 \leq N \leq 9$	822	778	323	0.195	-22.19	156	11
$-22.5 < M_r < -22.0$	$N \geq 10$	531	494	260	0.186	-22.22	134	6
$-22.0 < M_r < -21.5$	All	5830	5412	464	0.170	-21.73	181	276
$-22.0 < M_r < -21.5$	$0 \leq N \leq 3$	1253	1148	303	0.171	-21.72	198	77
$-22.0 < M_r < -21.5$	$4 \leq N \leq 9$	1905	1773	400	0.170	-21.73	192	77
$-22.0 < M_r < -21.5$	$N \geq 10$	732	686	256	0.166	-21.75	166	18
$-21.5 < M_r < -21.0$	All	6991	6477	697	0.144	-21.25	200	414
$-21.5 < M_r < -21.0$	$0 \leq N \leq 3$	1784	1633	385	0.143	-21.25	223	116
$-21.5 < M_r < -21.0$	$4 \leq N \leq 9$	2166	2009	414	0.144	-21.25	210	128
$-21.5 < M_r < -21.0$	$N \geq 10$	648	603	264	0.142	-21.25	199	22
$-21.0 < M_r < -20.5$	All	5111	4749	626	0.126	-20.78	231	424
$-21.0 < M_r < -20.5$	$0 \leq N \leq 3$	1425	1319	350	0.125	-20.77	237	130
$-21.0 < M_r < -20.5$	$4 \leq N \leq 9$	1446	1343	395	0.126	-20.78	223	112
$-21.0 < M_r < -20.5$	$N \geq 10$	488	463	205	0.125	-20.77	228	25
Magnitude	Redshift	Number	Used	S/N	$\langle z \rangle$	$\langle M_g \rangle$	$\sigma$ applied	
$M_g < -21.8$	$0.15 < z < 0.25$	297	276	184	0.210	-21.98	90	
$M_g < -21.8$	$0.25 < z < 0.35$	685	641	184	0.305	-21.99	51	
$M_g < -21.8$	$0.35 < z < 0.45$	1286	1200	169	0.403	-22.00	71	
$M_g < -21.8$	$0.45 < z < 0.50$	762	700	87	0.475	-22.01	139	

NOTES.—Column titled “Number” lists the number of objects that pass our morphology, luminosity, density, and color cuts. The column titled “Color reject” lists the number that passed the morphology, luminosity, and density cuts, but failed the color cut. The column titled “Used” lists the number actually used; some objects fail our spectral quality cuts on the amount of missing or masked data. The column titled “S/N” lists the average signal-to-noise ratio per pixel of spectrum (roughly 1 Å) in the stacked spectrum. The average redshift and absolute magnitude in each sample is given, as is the dispersion of the Gaussian required to smooth the average spectrum to a velocity dispersion of 325 km s<sup>-1</sup>. The sums of the 3 environment samples at a given luminosity do not equal the “All” environment sample because we exclude galaxies from the environment sample that fall less than 0.5h<sup>-1</sup> Mpc from the edge of the survey imaging.

### 3.3. Local density estimation

We wish to study the spectral properties of our galaxies as a function of their environment. As our spectra are of luminous galaxies, we do not have full spectroscopic coverage of the fainter neighbors. We therefore resort to counting nearby galaxies from the SDSS imaging data. This has the advantage that it is independent of the SDSS spectroscopic coverage, which of course is only partially complete, and that the same luminosity cuts can be applied to all galaxies. To include a poor-man’s photometric redshift scheme, we restrict the count to galaxies consistent with early-type colors at the appropriate redshift.

Given the spectroscopic redshift of a particular luminous galaxy, we calculate the angular scale corresponding to a transverse distance of 0.5h<sup>-1</sup> Mpc, the  $r$  band luminosity of an  $L^*$  passively-evolved early-type galaxy, and the  $g - i$  color of that galaxy. The last of these is based on the average color of the two evolving models in Eisenstein et al. (2001). We then count the number of galaxies that fall within 0.15 mag in  $g - i$  model color, within 1 mag brightward and 2 mag faintward in  $r_{\text{Petro}}$  flux, and between 0.03 and 0.5h<sup>-1</sup> Mpc in transverse distance. Primary galaxies that fall within 0.5h<sup>-1</sup> Mpc of the edge of the imaging sample are excluded from the environmental studies. This means that the samples for environment variations are smaller than those for luminosity variations (see Table 1).

This count of nearby early-type galaxies gives us an estimate of the local environment of our candidate. However, the statistic is noisy. With random positions inside the survey region, we find an average of 3.6 neighbors, nearly independent of redshift. The average number of neighbors around the actual galaxies increases with luminosity: 5.8, 5.7, 6.4, and 8.95 for luminosity bins of  $-21.0 < M_r < -20.5$ ,  $-21.5 < M_r < -21.0$ ,  $-22.0 < M_r < -21.5$ , and  $-22.5 < M_r < -22.0$ , respectively. Hence, while we have clear evidence that galaxies are clustered, the Poisson error on the background is not small relative to the average signal. We cannot make fine distinctions about the local density but instead can construct generously large bins that should be monotonic in their typical density.

For each luminosity bin in the MAIN sample, we divide the sample into three density bins—those with 10 or more neighbors, those with 4 to 9 neighbors, and those with 3 or fewer neighbors—for a total of 12 samples. While the dividing line between the samples will be blurred, with equivalent galaxies jumping the boundary due to background Poisson fluctuations, bins this large should be reasonably distinct as regards the actual (non-projected) density of the included galaxies.

## 4. THE AVERAGE SPECTRA

Figure 4 gives an example of the type of average spectrum we are analyzing. 365 spectra of luminous early-type galaxies in the redshift range  $0.30 < z < 0.35$  have been

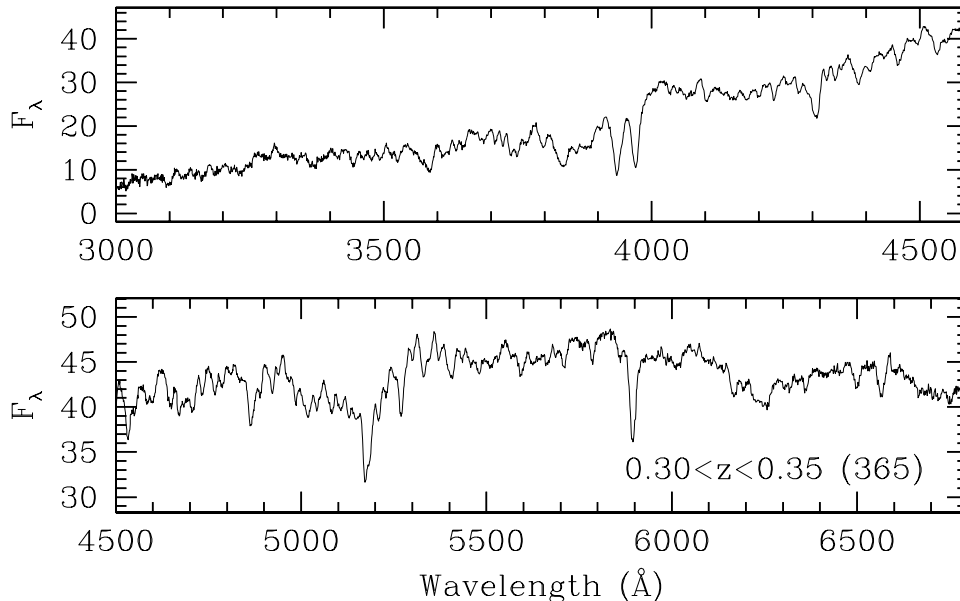


FIG. 4.— The average spectrum of 365 luminous red galaxies, selected as described in § 3.2, in the redshift range  $0.3 < z < 0.35$  over the rest-frame wavelength range of 3000Å to 6800Å. The noise and pixel scale are visible on the blue and red ends as a fine-scale roughness; in between, the noise per pixel is generally smaller than the thickness of the line. The vertical normalization is arbitrary.

used to produce this stacked spectrum. The wavelength range of 3000Å to 6800Å rest-frame is shown; this corresponds roughly to 4000Å to 9000Å in observed wavelength. Careful inspection of the blue and red ends reveals some noise on the pixel scale. In the blue, this is caused by the lower sensitivity of the spectrographs and of course the intrinsic faintness of early-type galaxies in the rest-frame UV. In the red, imperfect sky subtraction limits the performance. In between, the error per pixel is smaller than the thickness of the line. The velocity dispersion of the ensemble creates a visually obvious scale of the width of astrophysical features in the spectrum; comparing that width to the pixel scale revealed by the noise should convince the viewer that essentially all of the features in the spectrum are real. Nearly all of the average spectra we consider have higher signal-to-noise ratios than this one.

#### 4.1. Absorption line strengths

All of the average spectra in this paper are typical early-type galaxy spectra; they are dominated by the absorption line features found in the spectra of old stellar populations. This can be made quantitative with comparison to the V99 models via the sLick indices.

Broadly, the sLick index measurements (given in Table 2) are consistent with the conclusion that our sample is composed primarily of an old, metal-rich stellar population. However, there is a large scatter in the inferred ages or metallicities among different sLick indices; i.e., none of the V99 models is a good match to the total spectrum.

Figure 5 shows this graphically. In each panel, a sLick index based on H $\delta$  is plotted against one of various metal line indices. The measurements from 16 average spectra,

our luminosity and environment samples, are shown as square dots. The V99 models are shown as a grid of metallicity and age. Three metallicities ( $-0.4$ ,  $0$ , and  $+0.2$  dex relative to solar) and six ages (4, 5, 6.3, 8, 10, 12, and 15 Gyr) are shown. We will defer discussion of the trends in luminosity and environment until § 5; here our point is simply that no single V99 model matches all indices for a given spectrum.  $\alpha$ -elements (e.g., Mg b) tend to show higher metallicities, while iron-peak elements (e.g., Fe5270) show lower metallicities. This can be explained, at least in part, by a mismatch in chemical abundances. In particular, the Vazdekis models have solar abundance ratios and it appears that the average spectra show enhanced abundances for  $\alpha$ -process elements relative to iron-peak elements. This  $\alpha$ -enhancement has been noted previously (Worthey et al. 1992; Vazdekis 1999; Davies et al. 2001; Trager et al. 2000a; Proctor & Sansom 2002) and is expected for a stellar population that converts its gas entirely into stars rapidly, before type Ia supernovae have time to significantly pollute the interstellar medium with iron-peak elements.

The hydrogen Balmer lines have been widely used to try to disentangle metallicity and age estimation in old stellar systems (e.g., O’Connell 1976; Rose 1985; Worthey et al. 1994; Worthey & Ottaviani 1997; Vazdekis & Arimoto 1999). We study the H $\beta$ , H $\gamma$ , and H $\delta$  lines. For galaxies with velocity dispersions of 275 km s $^{-1}$ , the Vazdekis models predict that H $\beta$  sLick index is the least sensitive to metal content, while the H $\gamma$  and H $\delta$  sLick indices still carry significant metal dependence (in the sense that more metal-rich systems would be inferred to be younger). However, as we will see, H $\beta$  has some contamination from in-



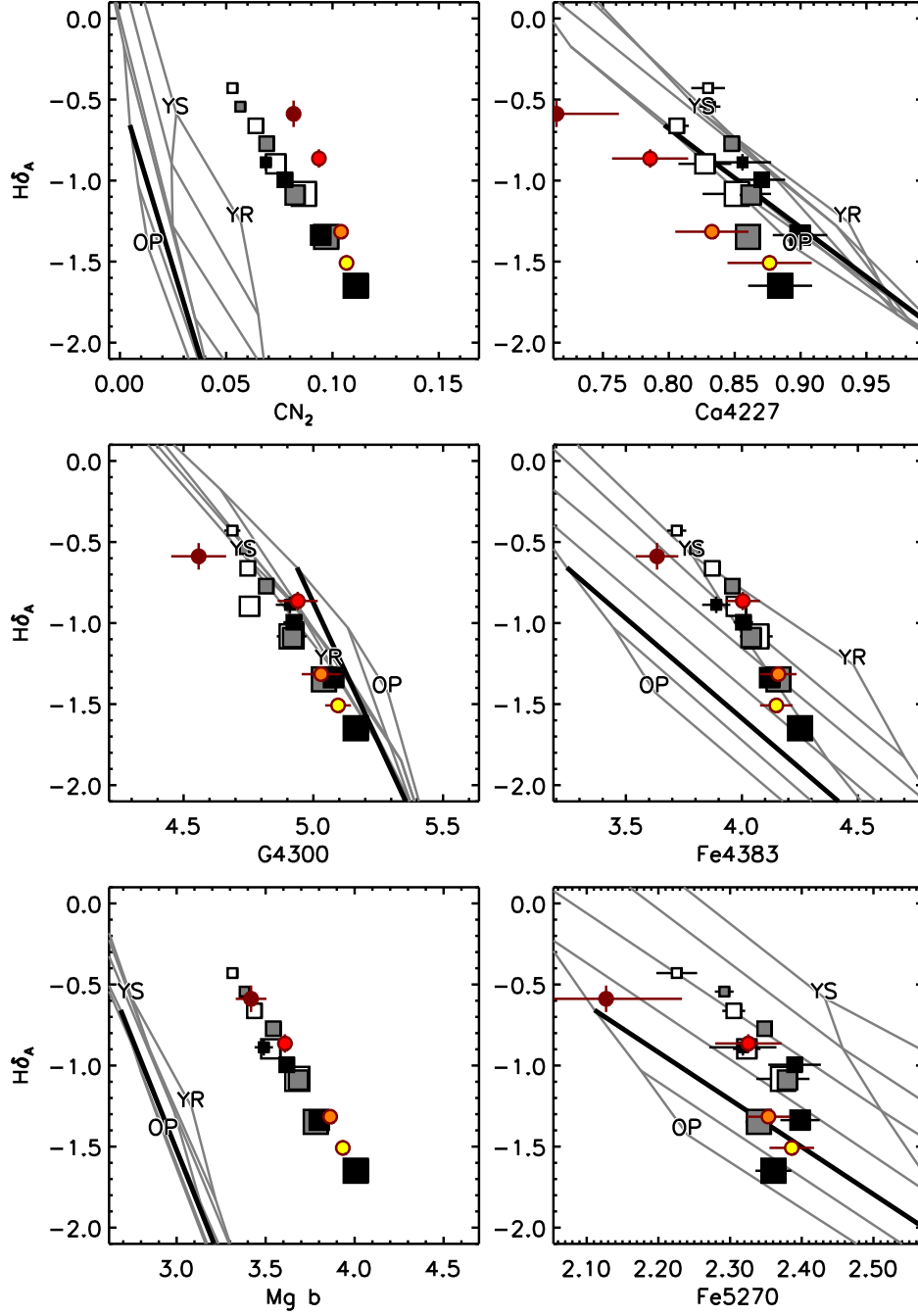


FIG. 5.— Each panel shows a plot of two sLick indices, with the  $H\delta_A$  index plotted against various metal indices. Points show the values measured from different samples. Squares indicate the environment sub-samples. Black squares are the  $N > 10$ , high-density sample. White squares are the  $N \leq 3$ , low-density sample. Grey squares are the  $4 \leq N \leq 9$ , intermediate-density sample. The size of the square indicates the luminosity of the sample, with the largest square being  $-22.5 < M_r < -22$  and the smallest square being  $-21 < M_r < -20.5$ . Circles indicate the LRG sample divided by redshift, with the darker color being higher redshift. Error bars in both indices are shown but are often smaller than the points. The line grid shows the predictions from the V99 model, as described in § 2.6. Three metallicities are shown ( $-0.4$ ,  $0$ , and  $+0.2$  dex relative to solar) and six different ages (4, 5, 6.3, 8, 10, 12, and 15 Gyr). The thicker line marks the 10 Gyr locus. The letters YS, YR, and OP indicate the ‘young, solar’, ‘young, metal-rich’, and ‘old, metal-poor’ boundaries of the grid.

terstellar emission lines and so we focus on  $H\delta$  and  $H\gamma$  indices, where the effect is negligible.

For  $H\delta$  and  $H\gamma$ , comparing the V99 models at solar metallicity suggests a relatively young age, roughly 5–6 Gyr, for a single-age burst (see the  $H\delta_A$  versus Fe4383 panel of Figure 5). All four indices ( $H\delta_A$ ,  $H\delta_F$ ,  $H\gamma_A$ , and  $H\gamma_F$ ) give similar ages. As usual, a higher metallicity would imply a younger age. Such age inferences are famously biased by the presence of young A and F stars. We therefore consider histories in which some fraction of the stars are indistinguishably old (we adopt 12.5 Gyr) while the rest are formed at a constant rate between 1 and 12.5 Gyrs (we exclude recent formation on the grounds that our color cut would exclude blue star forming galaxies), assuming solar metallicity throughout (a poor assumption, see Maraston & Thomas 2000). To match  $H\gamma$  and  $H\delta$ , one would need to form  $\sim 50\%$  of the stars in the continuous phase, which gives an average age of  $\sim 9$  Gyr.

$H\beta$  on the other hand implies an old age, above 12 Gyr for the solar-metallicity V99 model. The emission in the average spectrum (§ 4.2) undoubtedly makes this an upper limit. When correcting for non-zero velocity dispersions and line emission by the prescriptions of Trager et al. (1998, 2000a), we find  $H\beta$ , Mg  $b$ , Fe5270, and Fe5335 indices that fall comfortably within the  $z = 0$  locus found by Trager et al. (2000a), although our  $H\beta$  lines are slightly deeper (i.e., younger) than their median value.

Above all, however, we feel that the obvious failings of solar abundance ratio models to simultaneously fit multiple metal indices caution against any quantitative conclusion on the age of the stellar populations. The Balmer line indices are affected by metal absorption, and it may be that neglecting the  $\alpha$  to Fe abundance ratio differences skews the age inferences or disturbs the agreement between  $H\delta$  and  $H\beta$ .

#### 4.2. Emission-line components

In addition to generating the average spectrum, the PCA algorithm provides us with all of the spectral components that contribute significantly to the diversity (variance) of the spectra in our samples. There is a clear emission-line component that affects roughly 10% of the spectra. We isolate all variations from the “typical” spectrum by seeking outliers in the locus of PCA coefficients. In particular, noting that the PCA coefficients of most galaxies fall in a tight distribution near zero (save for the first component, which has a tight distribution with non-zero mean), we form the sample of galaxies that have all coefficients (excluding the first and as usual any beyond the 20th component) within some tolerance of zero. The numerical value of this threshold is meaningless without discussion of the normalization of the PCA eigenspectra, but visually it imposes a tight envelope around the cloud of points containing the bulk of the galaxies. It is likely that much of the scatter in this cloud is observational scatter. We call the selected galaxies the “median” sample. We then form the average spectrum of this sample and subtract that from the average spectrum of the full sample.

An example of the resulting spectra is shown in Figure 6. Here we have taken our MAIN sample bulge-dominated galaxies in the highest luminosity bin,  $-22.5 < M_r < -22$ . Only 5% of the galaxies fell in the outlier sample, although

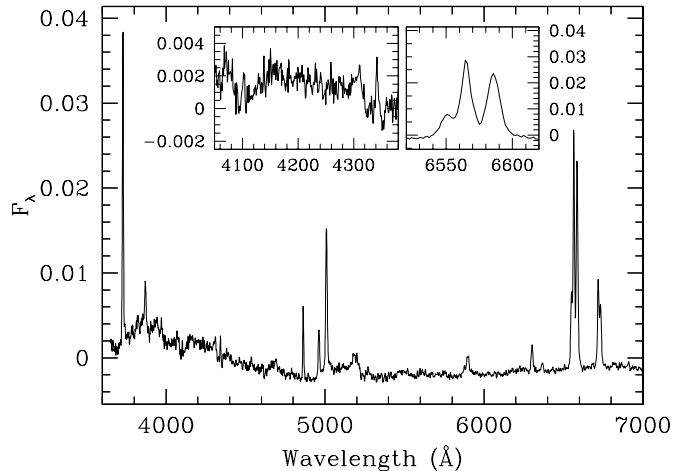


FIG. 6.— The difference spectrum of outliers from the locus of luminous bulge-dominated galaxies in the luminosity range  $-22.5 < M_r < -22$ . 5% of the galaxies whose PCA coefficients fall outside of the primary distribution of points are labeled as outliers. This spectrum is the change to the average spectrum from including or excluding these objects. The resulting spectrum shows a number of emission lines, with relative strengths characteristic of a LINER, as well as some alterations to some absorption lines, including the higher-order Balmer lines.

this fraction rises at lower luminosities (see Table 3). The residual spectrum has obvious emission lines, as well as reduced absorption at Na D and Mg  $b$ . There is a hint of additional absorption in the higher Balmer lines as well as an overall blue tilt. It is worth noting, however, that the differences between the average spectrum of all galaxies and the “median” sample are small, as one can see by comparing the vertical axes in Figures 6 and 8. The effects on the sLick indices are negligible, save for the stronger emission lines (e.g. [O III] and  $H\beta$ ).

We do not claim that this residual spectrum contains all of the line emission; clearly a baseline emission rate will not be included. However, if emission is the exception rather than the rule for these galaxies, then this residual spectrum will contain most of the emission. It is our impression that a few objects dominate the total emission strength. Note that the method will select all the objects with strong  $H\alpha$ , [O II], and/or [O III] emission; the weak emission at  $H\gamma$  and  $H\delta$  need not be detected in individual spectra for it to appear in the residual spectrum. Finally, it is important to note that the residual spectrum contains all deviations from the median, but it is not required that these deviations occur along a single “direction” in the space of PCA coefficients. While we detect emission and absorption, it is possible that different outlier galaxies contribute these in different proportions.

In detail, the emission-line spectrum satisfies most of the definitions of a LINER (Heckman 1980; Veilleux & Osterbrock 1987). [N II]  $\lambda 6583$ , [O I]  $\lambda 6300$ , and [S II]  $\lambda \lambda 6716, 6731$  are strong compared to  $H\alpha$ , while [O III]  $\lambda 5007$  is weak compared to  $H\beta$ . Of course, it is not straightforward to give a physical interpretation to this average spectrum. It is likely that the galaxies show a diversity of star formation and AGN emission mechanisms, and we would not claim that the average spectrum proves that star formation is negligible. Future work will explore the details of the emission line behavior of these early-type

galaxies.

Lower luminosity bulge-dominated galaxies show stronger emission-line components as well as a more obvious Balmer absorption component. This will be discussed in § 5.3.

### 5. VARIATIONS WITH LUMINOSITY AND ENVIRONMENT

We now will proceed to our primary task, to analyze the average spectra of luminous bulge-dominated galaxies as a function of luminosity and environment. Recall that, as described in §3, we break each of our 4 luminosity bins into 3 environment bins. We also analyze each of the 4 luminosity bins in its entirety.

There is a striking level of similarity among the average spectra of these subsamples. Dividing by redshift, luminosity, and environment always yields the same qualitative spectrum. However, we do find small but highly significant differences among the average spectra. In broad terms, the trends are similar to those found in previous work (e.g., Dressler et al. 1987; Bower et al. 1990; Guzman et al. 1991; Bender et al. 1993; Rose et al. 1994; Trager et al. 2000b; Bernardi et al. 2001).

#### 5.1. Variations in the *sLick* indices

Figures 5 and 7 show the spectral variations as a function of luminosity and environment as measured by the *sLick* indices. Lower luminosity galaxies or those in poorer environments have indices that would be interpreted as younger or more metal-poor. In some cases, notably the iron indices, the variations would be interpreted primarily as age. However, we are concerned that the poor match between the data and the models in other indices (e.g. Mg *b*) may cast doubt on such detailed interpretation.

The quantitative values of the *sLick* indices are presented in Table 2, along with their errors, and the V99 model predictions (where available). We also present the slopes of linear regressions versus luminosity, environment, and redshift within the sets of comparison samples. Slopes that are significant at  $3\text{-}\sigma$  are shown in boldface.

#### 5.2. A one-dimensional spectral space

A striking feature of Figures 5 and 7 is that the locus of values found in the luminosity and environment samples are nearly one-dimensional. In other words, with two different parameters at play, one might have expected the *sLick* indices to populate two-dimensional regions in these plots. Instead, the points fall (primarily) on tight curves, even for pairs of indices for which the models predict a separation of the effects of age and metallicity. This suggests that luminosity and environment control the same parameter in the average spectra. The H $\beta$  index is an exception, which we will discuss later.

To investigate this regularity, we took the 16 average spectra (12 from the luminosity/environment bins and 4 from the pure luminosity bins), subtracted the mean, and performed a PCA analysis on the residuals. No points were masked and no continua were subtracted, but as usual the spectra were smoothed to  $325 \text{ km s}^{-1}$  before performing the PCA. 89% of the variance in the 16 spectra was contained in the first PCA component, i.e., removing this component drops the rms variation from 1% to 0.3%. The mean spectrum and the first component of variation is

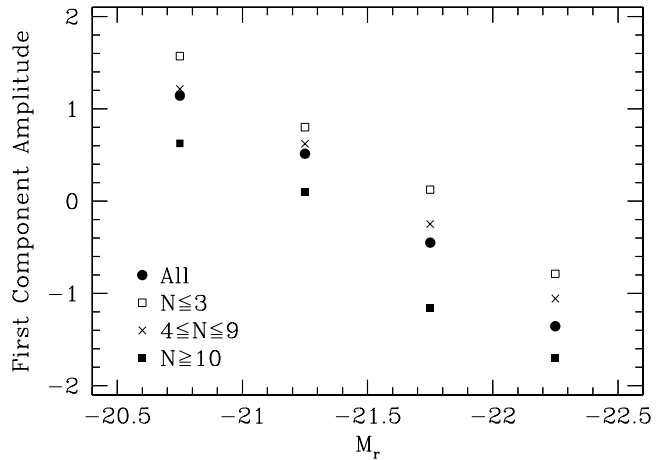


FIG. 9.— The amplitude of the first component of variation relative to the mean (these two spectra are shown in Fig. 8) as a function of luminosity for three different environment bins. The normalization of the spectral component was chosen so that the *rms* value of this amplitude was unity; as shown in Fig. 8, this corresponds to  $\sim 1\%$  variations in the spectra.

shown in Figure 8. The normalization of the first variation component relative to the mean is chosen so that the *rms* amplitude of the variation is unity. In other words, the relative normalization in Figure 8 is the typical spread in the 16 spectra, which is 1% *rms* of the mean.

The first component of variation is clearly a mix of emission and absorption lines. Emission at H $\alpha$ , H $\beta$ , [O II], [O III], [N II], and [S II] is visible. Higher-order Balmer lines are seen in absorption, and the strong Mg and Na absorption lines at 5175Å and 5900Å are varying in strength. The variation in the Mg line is slightly displaced to the red relative to the deepest part of the line in the mean spectrum; this indicates that blending of the lines can be important. Finally, there is a broadband tilt to the spectrum, in the sense that variations in the direction of extra nebular emission and stronger Balmer absorption correlate with a bluer spectrum, as one might expect.

The behavior at H $\delta$  and H $\gamma$  is of concern: although the variation spectrum appears to have extra absorption at these frequencies, the absorption troughs are wider than expected (compare the line shapes to those of the higher-order Balmer lines near 3800Å). In other words, we worry that other nearby metal lines may be impacting the H $\delta$  and H $\gamma$  *sLick* indices.

The second component of variation in the PCA analysis is smaller by a factor of 4. It is primarily broadband fluctuations, with a small amount of H $\alpha$  emission.

Figure 9 shows the amplitudes of the first component required by our 16 different samples. As expected, lower luminosity galaxies and those in poorer environments have more emission and Balmer absorption.

We stress that the information in Figure 8 goes well beyond the *sLick* indices. We have found the empirical primary direction of variation with respect to luminosity and environment for the ensemble of luminous, early-type galaxies over most of the optical range. While we are limited in the resolution available from hot stellar systems, there are hundreds of spectral elements measured to high signal-to-noise ratio in this spectrum. Matching these vari-

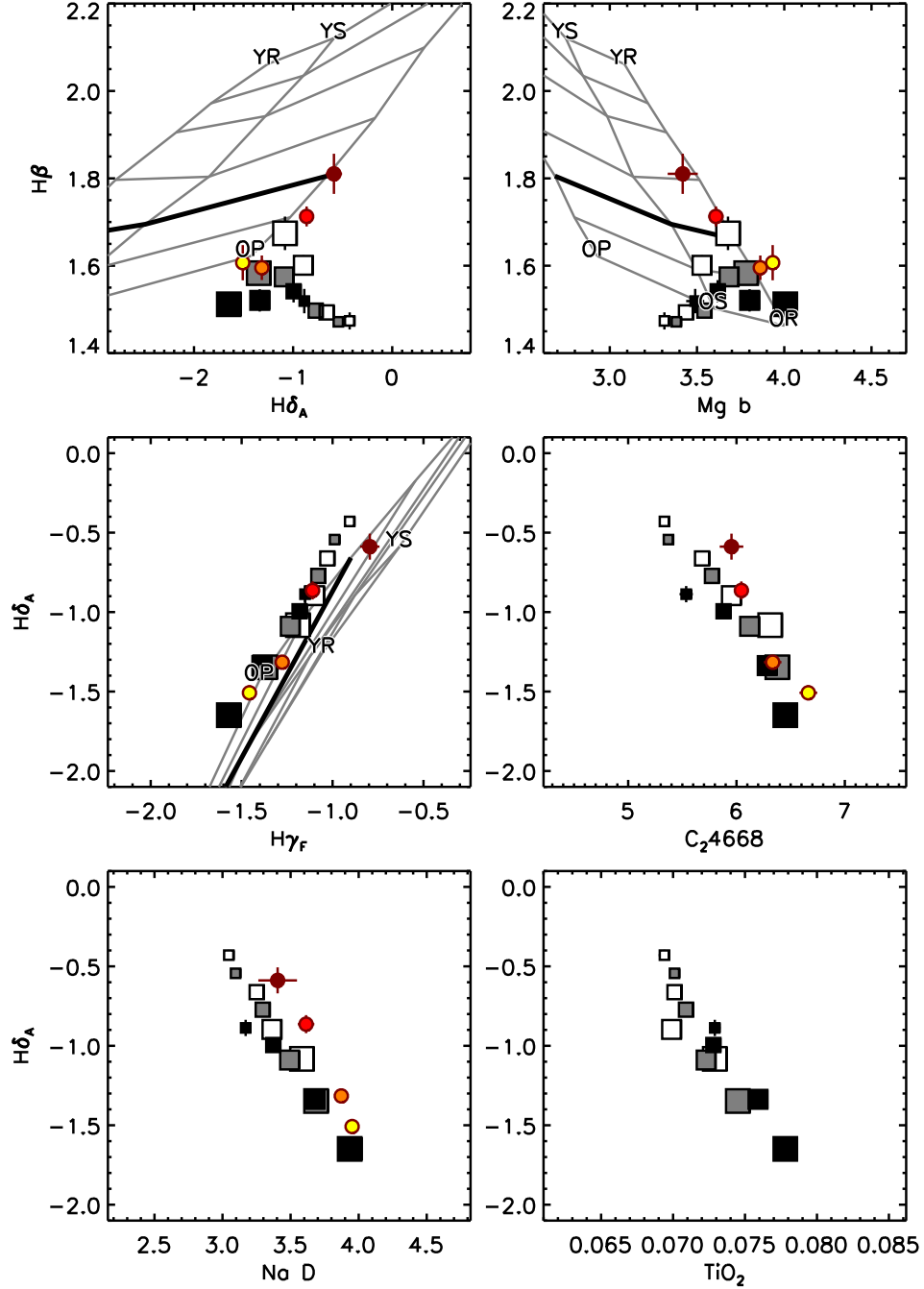


FIG. 7.— As Figure 5, each panel shows a plot of two sLick indices. The top two panels show the  $H\beta$  index against the  $H\delta_A$  and  $Mg_b$  indices. These show that  $H\beta$  does not follow a simple one-dimensional locus; it is unclear whether this is the result of emission line contamination. The lower four panels show the  $H\delta_A$  index against the  $H\gamma_F$  index and three metal-line indices plotted against the  $H\delta_A$  index. The grid of V99 models are absent in three panels where the index wavelength falls outside the wavelength range of the models.

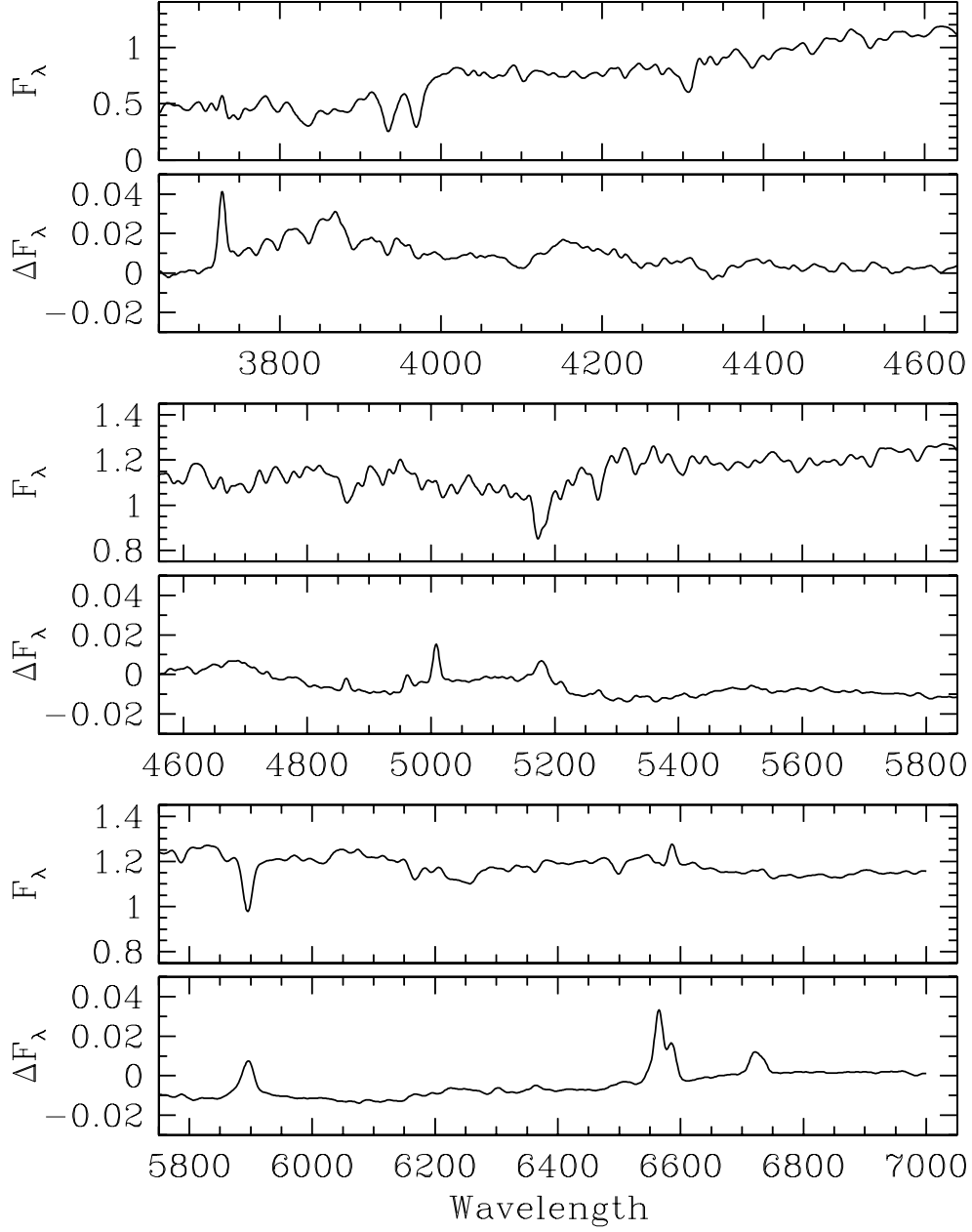


FIG. 8.— The average of the average spectra from all of the environmental and luminosity samples (note that this double counts some galaxies), along with the first component of variation between these 16 sets. This component accounts for 89% of the variance in the 16 spectra. The normalization of the first component of variation relative to the mean spectrum is set by the *rms* amplitude of this component. Higher components have very small amplitudes ( $\sim 0.002$ ) on this scale.

ations would be a stringent test for stellar population synthesis. We have not attempted more detailed comparisons to the models because it is clear that the available solar element abundance ratio models are a poor match to the mean spectrum.

As an aside, the fact that the first component of spectral variation contains 89% of the variance between the 16 spectra while being only 1% variation *rms* is a striking confirmation of the high signal-to-noise ratio of the average spectra. If these spectra had S/N of only 100 per pixel, then the PCA eigenspectra corresponding to this noise would have been comparable to the astrophysical variation, so that the first component would have only explained  $\sim 1/16$  of the variance. Hence, the signal-to-noise ratio of the spectra must considerably exceed 100 for errors that are not common to all the spectra. This is particularly remarkable given that no broadband modes were removed prior to this PCA analysis; indeed, much of the first component's variation is broadband, as it contains only 0.5% *rms* of variation when 4 broadband modes are removed.

### 5.3. Variations in emission-line components

In § 4.2, we isolated the spectral variations of outlier galaxies by using the PCA coefficients to identify the outliers and then considering the difference between the average spectrum of all the galaxies and the average spectrum of those in the “median” sample. We now consider these residual spectra as functions of luminosity and environment. We generally find that galaxies of lower luminosity and poorer environment have stronger emission line components.

In the case of  $H\gamma$  and  $H\delta$ , we clearly see small emission lines sitting in deeper absorption lines (Figure 6 inset), indicating that the residual spectrum contains both Balmer absorption from young stars and Balmer emission from young stars and active nuclei. We stress again that this superposition is a property of the composite of outliers and may reflect multiple populations of outliers from the “typical” old stellar spectrum.

To quantify the strength of these lines, we fit separate Gaussians to the emission and absorption lines, assuming that all emission lines in the spectrum have the same velocity width. The resulting line fluxes are shown in Table 3. Converting these to equivalent widths shows that the contribution to the  $H\gamma$  and  $H\delta$  indices are very small: a 15% effect on the inferred age in the worst case. We therefore infer that the  $H\gamma$  and  $H\delta$  indices are negligibly affected by emission in the full sample.

$H\beta$  on the other hand does seem to have significant emission, roughly enough to cancel out what must be non-negligible absorption. The two contributions are more difficult to disentangle, and it seems possible that the age inferred from  $H\beta$  would be significantly affected. The fact that  $H\delta$  and  $H\gamma$  are well-correlated with metal-line indices while  $H\beta$  has a lot of scatter may also be suggestive of emission in  $H\beta$ . However, it might indicate that the higher lines have significant contamination from metallicity variations.

$H\alpha$  has even stronger emission and the presence of strong [N II] makes it impossible to detect an absorption component. The line ratio of [N II] to  $H\alpha$  displays a increasing trend with luminosity and density, which may indicate an

decreasing role of star formation in driving the emission (Veilleux & Osterbrock 1987).

In general, the Balmer decrement is larger than expected from conventional predictions of the recombination spectrum. This may be caused by dust obscuration of the emission regions.

### 5.4. Selection biases

The interpretation of the spectral differences is subject to considerations of biases in the sample selection and analysis.

Fortunately, the comparison between samples from different environments is substantially immune to redshift-dependent effects, such as variations in the sample selection or change in physical spectroscopic aperture across redshift, because the redshift distributions of the three environment bins are nearly identical. Target selection and all aspects of the observations were done without consideration of the environment of the galaxies. The only significant effect is that galaxies in clusters tend to be more luminous. However, the 0.5 magnitude bin size in luminosity limits the shift in the mean luminosity between environment subsamples to less than 2% in the lower three luminosity samples and 4% in the most luminous sample (Table 1).

The comparison across luminosity, on the other hand, may include some biases in sample selection. First, there is a small shift in redshift (listed in Table 1 and shown in Figure 2) between the luminosity bins. If all samples were passively evolving, the most luminous galaxies would appear  $\sim 1$  Gyr younger than the least luminous relative to a fixed redshift comparison. Second, galaxies of different luminosities have different physical sizes, so that the spectroscopic fiber will include a different fraction of, e.g., the effective radius of the de Vaucouleurs model. Radial population gradients will therefore bias our results (McClure 1969; Munn 1992, and references therein). This effect is partially offset by the change in angular diameter distance with redshift. Finally, and most important, the lower luminosity bins almost certainly have more contamination from objects that would not be classified by eye as red, elliptical galaxies. Our morphology cut is relatively crude and does not include obvious mainstays of quantitative morphology such as bulge-disk decomposition and smoothness. It is not clear that equivalent samples are being selected at all luminosities or even that equivalent samples can be selected in principle. The difficulty of homogenizing stellar disk contributions could also bias the environmental subsamples because of the density-morphology relation.

### 5.5. Interpretation of absorption lines

Figures 5, 7, and 8 and Table 2 all demonstrate that there are statistically significant differences between the luminosity and environment subsamples. Table 2 displays the slopes and errors resulting from least-squares fits to each sLick index across luminosity and environment. Indices with more than  $3\text{-}\sigma$  detections of variation are shown in boldface. In particular, the  $H\delta$ , CN<sub>2</sub>,  $H\gamma$ , G4300, C<sub>2</sub>4668, Mg b, Na D, and TiO<sub>2</sub> indices all show strong variations.

In principle, such well detected variations should be able not only to determine age and mean metallicity shifts, but also to probe for variations in abundance ratios. Trippico



TABLE 3

EMISSION AND ABSORPTION LINE FLUXES

Magnitude	Environment	$F_{em}$	Emission								Absorption			
			H $\alpha$	H $\beta$	H $\gamma$	H $\delta$	[S II]	[N II]	[O III]	[O II]	H $\alpha$	H $\beta$	H $\gamma$	H $\delta$
$-22.5 < M_r < -22$	All	5%	0.31	0.073	0.028	0.017	0.21	0.40	0.17	0.28	...	0.005	0.065	0.074
	$N \geq 10$	7%	0.17	0.053	0.017	0.010	0.15	0.32	0.11	0.19	...	0.005	0.019	0.012
	$4 \leq N \leq 9$	7%	0.34	0.086	0.033	0.017	0.22	0.40	0.11	0.27	...	0.052	0.098	0.106
	$0 \leq N \leq 3$	6%	0.22	0.067	0.024	0.010	0.16	0.35	0.35	0.25	...	...	0.039	0.293
$-22 < M_r < -21.5$	All	8%	0.64	0.133	0.047	0.026	0.33	0.62	0.33	0.36	...	0.022	0.137	0.128
	$N \geq 10$	7%	0.37	0.073	0.021	0.015	0.20	0.30	0.13	0.20	...	0.039	0.120	0.117
	$4 \leq N \leq 9$	7%	0.62	0.124	0.049	0.031	0.33	0.57	0.39	0.39	...	0.009	0.133	0.140
	$0 \leq N \leq 3$	8%	0.65	0.125	0.048	0.019	0.30	0.58	0.26	0.32	0.061	0.032	0.187	0.139
$-21.5 < M_r < -21$	All	10%	1.02	0.207	0.073	0.035	0.42	0.86	0.41	0.41	...	0.052	0.239	0.225
	$N \geq 10$	11%	0.73	0.143	0.060	0.030	0.33	0.66	0.33	0.39	...	...	0.158	0.153
	$4 \leq N \leq 9$	10%	0.82	0.172	0.062	0.022	0.35	0.68	0.27	0.35	...	0.045	0.254	0.198
	$0 \leq N \leq 3$	11%	1.10	0.216	0.078	0.037	0.43	0.92	0.43	0.41	...	0.069	0.255	0.246
$-21 < M_r < -20.5$	All	12%	1.34	0.289	0.106	0.052	0.53	1.03	0.58	0.51	...	0.086	0.350	0.334
	$N \geq 10$	10%	0.85	0.185	0.078	0.046	0.43	0.79	0.51	0.49	...	0.009	0.180	0.173
	$4 \leq N \leq 9$	22%	1.26	0.270	0.096	0.046	0.47	0.96	0.40	0.42	...	0.114	0.328	0.294
	$0 \leq N \leq 3$	20%	1.26	0.264	0.097	0.045	0.50	0.93	0.47	0.46	...	0.076	0.343	0.325
Continuum $F_\lambda$ , units $\text{\AA}^{-1}$			1.20	1.14	0.92	0.75	1.15	1.2	1.10	0.46	1.20	1.14	0.92	0.75

NOTES.—Emission line strengths computed from the residual spectrum formed by the difference of the average spectrum and the “median” spectrum.  $F_{em}$  is the fraction of spectra that were declared as outliers and therefore omitted from the “median” spectrum. The higher-order Balmer lines are also seen to be in absorption; we fit a broad absorption Gaussian and a narrow emission Gaussian. The results are quoted as line fluxes in arbitrary units; the  $F_\lambda$  of the continuum is also given (in units of flux per  $\text{\AA}$ ). Equivalent widths can be found by dividing the line flux by the continuum  $F_\lambda$ . [S II] is a sum of the 6731 $\text{\AA}$  and 6716 $\text{\AA}$  lines, [N II] is a sum of the 6548 $\text{\AA}$  and 6583 $\text{\AA}$  lines, [O III] is only the 5007 $\text{\AA}$  line, and [O II] is the sum of the 3726 $\text{\AA}$  and 3729 $\text{\AA}$  lines.

& Bell (1995, hereafter TB95) calculate the variation in Lick indices induced by changes in the abundances of individual elements for 3 specific model stars. This grid of abundances and stars is too sparse to interpret the observed differences in our data. Nevertheless, if one adopts the overly simple model in which the TB95 cool giant and hot dwarf models are combined in arbitrary ratio with abundance variations allowed in groups of C & N, O,  $\alpha$  elements, and iron peak elements, and then resolves our observed index variations against these 5 vectors of model variations, then one finds that the variations amongst our spectra are best described by variations in the  $\alpha$  element abundance. Of course, age variations are available to this model only in so far as they could be mapped to changes in the giant to dwarf ratio. As an additional caveat (were there not enough already!), we note that the TB95 Lick indices are quoted at zero velocity dispersion while our variations are at 275  $\text{km s}^{-1}$ .

The indication that abundance ratio variations may be the controlling parameter in the spectral variation with luminosity and environment is intriguing. We believe that this hint should offer strong encouragement for the construction of spectral models of stellar populations with non-solar abundance ratios (e.g. Thomas et al. 2002).

## 6. AVERAGE SPECTRUM VS COSMIC TIME

Whereas our comparison of MAIN samples was all at low redshift, our LRG sample spans a large range in redshift,  $0.15 < z < 0.50$ , with galaxies that are similar in luminosity and rest-frame color. We can therefore look for the evolution of the average spectrum across cosmic

time. We divide the galaxies into 4 separate redshift bins:  $0.15 < z < 0.25$ ,  $0.25 < z < 0.35$ ,  $0.35 < z < 0.45$ , and  $0.45 < z < 0.50$ .

While the selected galaxies are luminous early-types at all redshift, there are subtle redshift dependences in the selection. For example, the fine details of the rest-frame luminosity-color region imposed at each redshift by the LRG selection will have mild redshift dependences (Figure 3). At this point, we have not assessed these because of uncertainties in the appropriate  $k$ -corrections and evolution corrections as well as the need to model the effect of the *noise* in the observed colors and magnitudes on the sample selection. Detailed modelling of these selection effects is now underway.

To first order, the galaxies in each bin should be similar, in the sense that a passively-evolving old galaxy would be in all the samples. However, the physical aperture of our 3'' diameter spectroscopic fiber is increasing with redshift, so that we are including more of the light of the higher redshift galaxies. If galaxies have older or more metal-rich stellar populations near their centers, then the higher redshift objects will be biased to look younger or more metal-poor. Of course, the size of such effects is bounded by the weakness of color gradients in giant elliptical galaxies (Franx et al. 1989; Peletier et al. 1990; Michard 2000) and by the fact that we observe the luminosity-weighted spectrum within the physical aperture.

The sLick indices measured for these average spectra are given in Table 2 and plotted as circles in Figures 5 and 7. The results show a clear dependence on redshift. Were this difference due only to age, the higher redshift

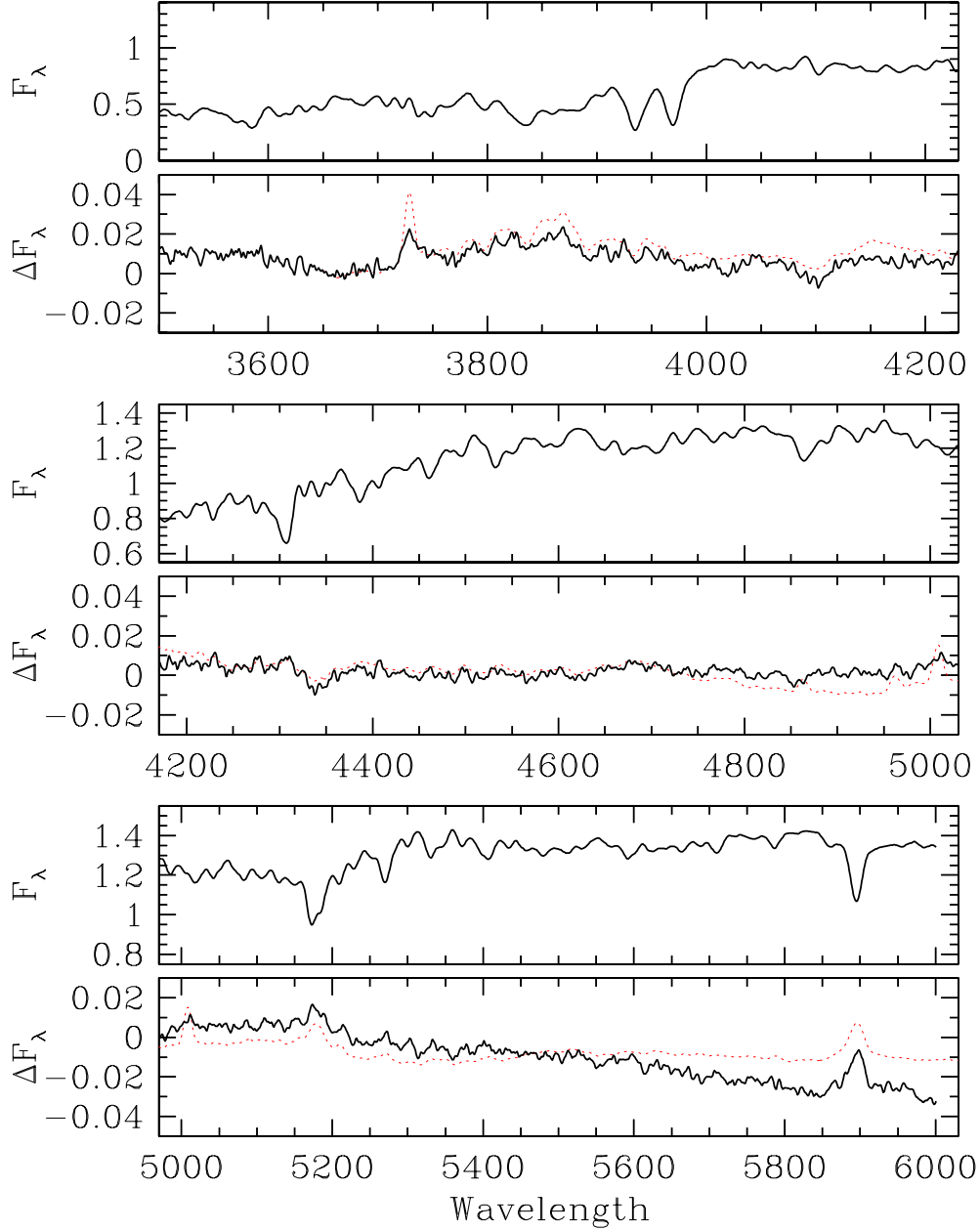


FIG. 10.— The average of the average spectra from all of the redshift samples along with the least-squares variation per 0.1 in redshift. The sign of the variation is such that one should add the variation spectrum to the mean when considering higher redshifts. The first component variation spectrum from Figure 8 is shown for comparison (*dotted line*). The relative normalization of the two variation spectra is arbitrary. The broadband offsets of the redshift variation spectrum should not be trusted because of spectrophotometry uncertainties; comparing fixed rest-frame wavelengths across redshift requires accurate spectrophotometry across a significant range of observed wavelengths, whereas the comparisons across environment and luminosity were less demanding of this. The redshift variation spectrum has more small-scale noise in part because the more luminous galaxies required less smoothing to reach a velocity dispersion of  $325 \text{ km s}^{-1}$ , thereby including more photon noise. Simulation of the noise indicates that, for example, the three largest features between  $4225\text{\AA}$  and  $4325\text{\AA}$  are significant at roughly  $5\text{-}\sigma$  confidence, while the features between  $4150\text{\AA}$  and  $4200\text{\AA}$  are only marginally significant.

galaxies would be younger by  $\sim 3$  Gyr, with some variation with index. This is consistent with concordance cosmology prediction of  $\sim 2.5$  Gyr. In the Figures, one should note that the results do not in all cases lie along the locus defined by the low-redshift luminosity and environment variations. If we view the redshift sample as defining the true time derivative of a metal-rich passively evolving population, then the luminosity and environment dependences may require abundance variations.

We next consider the variations of the full spectrum across redshift. We take the four average spectra, subtract the mean, and compute the least-squares slope for each pixel as a function of the central redshift of each spectrum. The vector of slopes is the spectrum of ordered variations within this set of four spectra. The highest redshift average spectra has noise roughly twice as large as the others, so we downweight it by a factor of 4 in the least-squares fitting. We normalize the slope to a difference of 0.1 in redshift. The PCA analysis of § 5.2 yields a similar variation spectrum to this least-squares method.

The resulting mean and variation spectra are shown in Figure 10. The variation spectrum shows more noise than the equivalent spectrum in the environment/luminosity comparison. This is partially because the highest redshift average spectra are noisier, but it is also because the LRG sample spectra required less smoothing to match to  $325 \text{ km s}^{-1}$  than the MAIN sample spectra. Despite this, many features in the variation spectrum are well detected. We assess the significance by creating realizations of the noise of the original spectra, smoothing, and applying the least-squares analysis. The smaller features in the variation spectrum are not significant, but features such as the three peaks between  $4225\text{\AA}$  and  $4325\text{\AA}$  are clearly significant. Further SDSS data should make interesting improvements in the signal-to-noise ratio of these spectra.

The variation spectrum shows strong alterations to absorption features at  $\text{H}\delta$ ,  $\text{H}\gamma$ ,  $\text{Mg } b$ , and  $\text{Na D}$ , as well as weaker changes to other lines.  $\text{Mg } b$  and  $\text{Na D}$  are shallower at higher redshift, while the two Balmer lines are deeper. Little hint of emission lines is found, save for  $[\text{O II}]$ , probably in part because the galaxies in the LRG sample are considerably more luminous than those in the MAIN sample. Overlaying the component of variation from the environment and luminosity analysis shows matching trends in the strongest features but imperfect agreement in the amplitudes of variations in different lines. Hence, the two variation spectra (in this section and § 5.2) represent two different combinations of age and metallicity; one might speculate that the redshift variation is dominantly due to age.

## 7. ULTRAVIOLET AVERAGE SPECTRUM

In Figure 11, we present the composite UV spectrum from our highest redshift galaxies, 726 luminous, red galaxies at  $0.47 < z < 0.55$ . Many absorption lines are detected, although the signal-to-noise ratio is poor at the bluest wavelengths because of the dropping efficiency of the SDSS spectrographs shortward of  $4000\text{\AA}$ . The  $2900\text{\AA}$  and  $2640\text{\AA}$  spectral breaks are clearly visible, as are the strong Mg lines at  $2796\text{\AA}$  and  $2852\text{\AA}$ . Using the definitions of Spinrad et al. (1997), we measure the strengths of these breaks to be  $B(2640) = 1.33 \pm 0.06$  and  $B(2900) = 1.41 \pm 0.04$ .

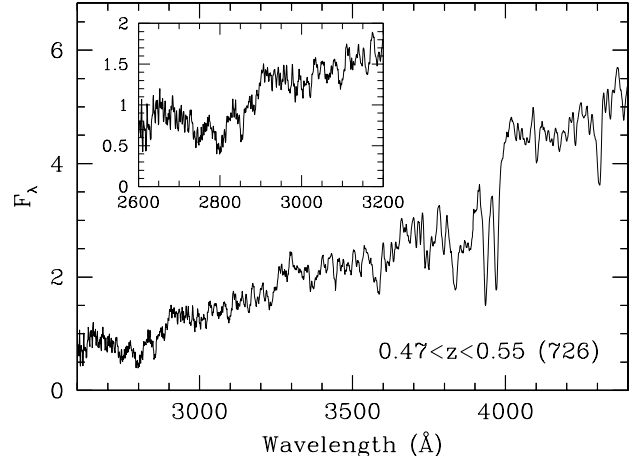


FIG. 11.— Average UV spectrum of 726 luminous, red galaxies at  $0.47 < z < 0.55$ . The inset shows an expansion of the bluest region of the spectrum. The  $2900\text{\AA}$  and  $2640\text{\AA}$  spectral breaks are clearly visible, as are the interstellar Mg lines at  $2796\text{\AA}$  and  $2852\text{\AA}$ . The vertical normalization is arbitrary.

The strengths of the UV breaks suggest that the UV spectrum has contributions from F-type stars (Spinrad et al. 1997; Fioc & Rocca-Volmerange 1997). Such stars can be present in the spectrum because either (a) there has been some star formation within the previous few Gyr, or (b) there is enough metallicity range among stars in the composite spectrum that there are old, F-type stars, either dwarfs or giants. Both explanations are plausible; we expect some ongoing star formation even among these old stellar populations, and we expect a wide metallicity range.

## 8. SUMMARY AND CONCLUSIONS

We have defined samples of luminous, red, bulge-dominated galaxies from the SDSS that represent controlled variations in luminosity, environment, and redshift. We have focused entirely on luminous galaxies, roughly  $L^*$  and above. The samples are a nearly complete representation of the most massive galaxies in the local universe.

We have computed luminosity-weighted average spectra so as to probe the aggregate stellar populations of these galaxies. The spectra indicate fairly old, metal-rich stellar populations that are enhanced in  $\alpha$  elements relative to iron-peak elements. Our primary goal has been to compare the relative differences in the populations as a function of luminosity, environment, and redshift. We find that the spectral variations across luminosity and environment are nearly a one-dimensional set. With a velocity-broadened form of the Lick indices, most index-index comparisons track a one-dimensional locus despite having two independent parameters (luminosity and environment). This is true even for pairs of indices that are predicted to split the familiar age-metallicity degeneracy. We find some indication that the controlling parameter of the variation may be the  $\alpha$ -to-Fe abundance ratio. Our results include not simply a vector of sLick index offsets, but a full resolution spectrum of the variation that includes over a hundred clearly visible lines.

We compared the average spectra directly to models

from V99, analyzing these model spectra identically to our data, and find that the variations are plausible even if the mean values of the indices may be shifted. More luminous galaxies, lower redshift galaxies, or those in denser environments would be interpreted as more metal-rich or older. However, we stress that the obviously non-solar  $\alpha$  to iron-peak ratio in our data probably invalidate any detailed interpretation of the differences with the solar-abundance-ratio models of V99.

We hope that the detail available in these spectra and their derivatives with luminosity, environment, and redshift will be a stimulus to detailed, full-resolution modelling of  $\alpha$ -enhanced, super-solar stellar populations. The spectra are available in electronic form as an on-line attachment to this paper.

We thank Jim Peebles, Scott Trager, and Ann Zabludoff for useful conversations and the referee for helpful comments. D.J.E. thanks NYU for hospitality while a portion of this research was completed. D.J.E. was supported by National Science Foundation (NSF) grant AST-0098577, by Hubble Fellowship grant #HF-01118.01-99A from the Space Telescope Science Institute, which is operated by the Association of Universities for Research in Astronomy, Inc, under NASA contract NAS5-26555, and by a Alfred P. Sloan Research Fellowship. D.W.H. was partially supported by NSF grant 0101738 and NASA contract NAG5-11669. This research made use of the NASA Astrophysics Data System.

Funding for the creation and distribution of the SDSS Archive has been provided by the Alfred P. Sloan Foundation, the Participating Institutions, the National Aeronautics and Space Administration, the National Science Foundation, the U.S. Department of Energy, the Japanese Monbukagakusho, and the Max Planck Society. The SDSS Web site is <http://www.sdss.org/>.

The SDSS is managed by the Astrophysical Research Consortium (ARC) for the Participating Institutions. The Participating Institutions are The University of Chicago, Fermilab, the Institute for Advanced Study, the Japan Participation Group, The Johns Hopkins University, Los Alamos National Laboratory, the Max-Planck-Institute for Astronomy (MPIA), the Max-Planck-Institute for Astrophysics (MPA), New Mexico State University, Princeton University, the United States Naval Observatory, and the University of Washington.

## REFERENCES

- Baldry, I.K., et al. 2002, *ApJ*, 569, 582  
 Barnes, J.E., & Hernquist, L. 1992, *ARA&A*, 30, 705  
 Baugh, C., Cole, S., & Frenk, C.S. 1996, *MNRAS*, 283, 1361  
 Bender, R., Burstein, D., & Faber, S.M. 1993, *ApJ*, 411, 153  
 Bender, R., & Saglia, R.P. 1999, *Galaxy Dynamics*, ASP Conference Series 182, ed. D.R. Merritt, M. Valluri, & J.A. Sellwood (San Francisco: ASP); [astro-ph/9811416](http://astro-ph/9811416)  
 Bernardi, M., et al. 2001, *AJ*, submitted; [astro-ph/0110344](http://astro-ph/0110344)  
 Blanton, M.R., et al., 2001a, *AJ*, 121, 2358  
 Blanton, M.R., Lupton, R.H., Maley, F.M., Young, N., Zehavi, I., Loveday, J., 2001b, *AJ*, in press  
 Bower, R.G., Ellis, R.S., Rose, J.A., & Sharples, R.M. 1990, *AJ*, 99, 530  
 Bower, R.G., Lucey, J.R., & Ellis, R.S. 1992, *MNRAS*, 254, 601  
 Bruzual, G., & Charlot, S. 2001  
 Charlot, S., Worthey, G., & Bressan, A. 1996, *ApJ*, 457, 625  
 Davies, R.L., Sadler, E.M., & Peletier, R.F. 1993, *MNRAS*, 262, 650  
 Davies, R.L., Kuntschner, H., Emsellem, E., Bacon, R., Bureau, M., Carollo, C.M., Copin, Y., Miller, B.W., Monnet, G., Peletier, R.F., Verolme, E.K., de Zeeuw, P.T. 2001, *ApJ*, 548, L33  
 Djorgovski, S., & Davis, M. 1987, *ApJ*, 313, 59  
 Dressler, A., Lynden-Bell, D., Burstein, D., Davies, R.L., Faber, S.M., Terlevich, R.J., & Wegner, G. 1987, *ApJ*, 313, 42  
 Eisenstein, D.J., et al., 2001, *AJ*, 122, 2267  
 Faber, S.M. 1972, *A&A*, 20, 361  
 Faber, S.M. 1973, *ApJ*, 179, 731  
 Faber, S. M., Friel, E. D., Burstein, D., & Gaskell, C. M. 1985, *ApJS*, 57, 711  
 Fioc, M., & Rocca-Volmerange, B. 1997, *A&A*, 326, 950  
 Franx, M., Illingworth, G., & Heckman, T. 1989, *AJ*, 98, 538  
 Franx, M. 1995, *IAU Symp.* 164: Stellar Populations, 164, 269  
 Fukugita, M., Hogan, C.J., & Peebles, P.J.E., 1998, *ApJ*, 503, 518  
 Fukugita, M., Ichikawa, T., Gunn, J.E., Doi, M., Shimasaku, K., & Schneider, D.P., 1996, *AJ*, 111, 1748  
 González, J. 1993, Ph.D. thesis, Univ. California, Santa Cruz  
 Gunn, J.E., Stryker, L.L., & Tinsley, B.M. 1981, *ApJ*, 249, 48  
 Gunn, J.E., et al., 1998, *AJ*, 116, 3040  
 Guzmán, R., Lucey, J.R., Carter, D., Terlevich, R.J. 1992, *MNRAS*, 257, 187  
 Heckman, T.M. 1980, *A&A*, 87, 152  
 Hogg, D.W., Finkbeiner, D.P., Schlegel, D.J., & Gunn, J.E. 2001, *AJ*, 122, 2129  
 Hogg, D.W., et al., 2002, *AJ*, 124, 646  
 James, P.A., & Mobasher, B. 1999, *MNRAS*, 306, 199  
 Kauffmann, G. 1996, *MNRAS*, 281, 487  
 Kauffmann, G., & Charlot, S. 1998, *MNRAS*, 294, 705  
 Kormendy, J. & Djorgovski, S. 1989, *ARA&A*, 27, 235  
 Lupton, R., Gunn, J.E., Ivezić, Z., Knapp, G.R., Kent, S., & Yasuda, N. 2001, in *ASP Conf. Ser.* 238, *Astronomical Data Analysis Software and Systems X*, ed. F. R. Harnden, Jr., F. A. Primini, and H. E. Payne (San Francisco: Astr. Spc. Pac.); [astro-ph/0101420](http://astro-ph/0101420)  
 Lupton, R.H. et al., 2002, in preparation  
 Maraston, C., & Thomas, D. 2000, *ApJ*, 541, 126  
 McClure, R.D. 1969, *AJ*, 74, 50  
 Michard, R. 2000, *A&A*, 360, 85  
 Munn, J.A. 1992, *ApJ*, 399, 444  
 O'Connell, R.W. 1976, *ApJ*, 206, 370  
 Oke, J. B. & Sandage, A. 1968, *ApJ*, 154, 21  
 Paquet, A. 1994, PhD thesis, University of Heidelberg  
 Peletier, R.F., Davies, R.L., Illingworth, G.D., Davie, L.E., & Cawson, M. 1990, *AJ*, 100, 1091  
 Petrosian, V., 1976, *ApJ*, 209, L1  
 Pier, J. R., et al. 2002, *AJ*, submitted  
 Poggianti, B.M., Bridges, T.J., Mobasher, B., Carter, D., Doi, M., Iye, M., Kashikawa, N., Komiyama, Y., Okamura, S., Sekiguchi, M., Shimasaku, K., Yagi, M., & Yasuda, N. 2001, *ApJ*, 562, 689  
 Proctor, R.N., & Sansom, A.E. 2002, *MNRAS*, 333, 517  
 Roberts, M. S. & Haynes, M. P. 1994, *ARA&A*, 32, 115  
 Rose, J.A. 1985, *AJ*, 90, 1927  
 Rose, J.A., Bower, R.G., Caldwell, N., Ellis, R.S., Sharples, R.M., & Teague, P. 1994, *AJ*, 108, 2054  
 Schlegel, D. J., Finkbeiner, D. P. & Davis, M. 1998, *ApJ*, 500, 525  
 Shimasaku, K., et al. 2001, *AJ*, 122, 1238  
 Smith, J. A., Tucker, D. L. et al. 2002, *AJ*, 123, 2121  
 Spinrad, H., Dey, A., Stern, D., Dunlop, J., Peacock, J., Jimenez, R., & Windhorst, R. 1997, *ApJ*, 484, 581  
 Stoughton, C. et al. 2002, *AJ*, 123, 485  
 Strateva, I. et al. 2001, *AJ*, 122, 1861  
 Strauss, M.A., et al., 2002, *AJ*, 124, 1810  
 Tammann, G.A., Yahil, A., & Sandage A., 1979, *ApJ*, 234, 775  
 Tantalo, R., Chiosi, C., & Bressan, A. 1998, *A&A*, 333, 419  
 Terlevich, A.I., Kuntschner, H., Bower, R.G., Caldwell, N., Sharples, R.M. 1999, *MNRAS*, 310, 445  
 Thomas, D., Maraston, C., & Bender, R. 2002, [astro-ph/0202166](http://astro-ph/0202166)  
 Trager, S. C., Worthey, G., Faber, S. M., Burstein, D., & Gonzalez, J. J. 1998, *ApJS*, 116, 1  
 Trager, S.C., Faber, S.M., Worthey, G., & González, J.J. 2000a, *AJ*, 119, 1645  
 Trager, S.C., Faber, S.M., Worthey, G., & González, J.J. 2000b, *AJ*, 120, 165  
 Trippico, M.J., & Bell, R.A. 1995, *AJ*, 110, 3035 (TB95)  
 van Dokkum, P. G. & Franx, M. 2001, *ApJ*, 553, 90  
 Vazdekis, A. 1999, *ApJ*, 513, 224 (V99)  
 Vazdekis, A., & Arimoto, N. 1999, *ApJ*, 525, 144  
 Veilleux, S., & Osterbrock, D.E. 1987, *ApJS*, 63, 295  
 Visvanathan, N., & Sandage, A. 1977, *ApJ*, 216, 214  
 Worthey, G., Faber, S. M., & Gonzalez, J. J., 1992, *ApJ*, 398, 69  
 Worthey, G., Faber, S. M., Gonzalez, J. J., & Burstein, D. 1994, *ApJS*, 94, 687  
 Worthey, G. & Ottaviani, D. L. 1997, *ApJS*, 111, 377  
 Worthey, G. 1998, *PASP*, 110, 888  
 York, D.G., et al. 2000, *AJ*, 120, 1579

TABLE 2

SLICK INDICES ON AVERAGE SPECTRA

Magnitude	Environment/ Redshift	H $\delta_A$ Å	H $\delta_F$ Å	CN <sub>2</sub> mag	Ca4227 Å	H $\gamma_A$ Å	H $\gamma_F$ Å	G4300 Å
$-22.5 < M_r < -22.0$	All	-1.347 (19)	0.301 (13)	0.0970 (5)	0.860 (10)	-5.508 (17)	-1.371 (11)	5.041 (22)
$-22.0 < M_r < -21.5$	All	-1.089 (14)	0.437 (10)	0.0824 (5)	0.862 (8)	-5.224 (12)	-1.233 (8)	4.920 (18)
$-21.5 < M_r < -21.0$	All	-0.772 (13)	0.575 (10)	0.0690 (5)	0.848 (6)	-4.915 (13)	-1.079 (8)	4.818 (14)
$-21.0 < M_r < -20.5$	All	-0.544 (19)	0.650 (14)	0.0566 (4)	0.831 (8)	-4.729 (17)	-0.989 (12)	4.735 (19)
Slope per mag		<b>-0.552</b>	<b>-0.242</b>	<b>+0.0267</b>	+0.021	<b>-0.536</b>	<b>-0.264</b>	<b>+0.203</b>
Error		0.016	0.012	0.0004	0.008	0.015	0.010	0.018
$-22.5 < M_r < -22.0$	$N \geq 10$	-1.649 (37)	0.189 (26)	0.1109 (13)	0.884 (24)	-5.818 (32)	-1.571 (20)	5.163 (39)
$-22.5 < M_r < -22.0$	$4 \leq N \leq 9$	-1.259 (23)	0.334 (16)	0.0925 (11)	0.870 (21)	-5.447 (29)	-1.349 (19)	5.011 (39)
$-22.5 < M_r < -22.0$	$0 \leq N \leq 3$	-1.082 (47)	0.408 (34)	0.0865 (11)	0.852 (26)	-5.170 (44)	-1.191 (29)	4.916 (57)
$-22.5 < M_r < -22.0$	$N$ slope	<b>-0.599</b>	<b>-0.231</b>	<b>+0.0236</b>	+0.033	<b>-0.662</b>	<b>-0.389</b>	<b>+0.256</b>
	Error	0.059	0.042	0.0017	0.036	0.054	0.035	0.068
$-22.0 < M_r < -21.5$	$N \geq 10$	-1.337 (32)	0.329 (23)	0.0944 (11)	0.900 (20)	-5.503 (29)	-1.389 (20)	5.078 (40)
$-22.0 < M_r < -21.5$	$4 \leq N \leq 9$	-1.069 (24)	0.424 (18)	0.0809 (7)	0.840 (9)	-5.264 (20)	-1.258 (13)	4.946 (22)
$-22.0 < M_r < -21.5$	$0 \leq N \leq 3$	-0.897 (32)	0.527 (23)	0.0733 (11)	0.827 (20)	-4.982 (23)	-1.099 (15)	4.754 (31)
$-22.0 < M_r < -21.5$	$N$ slope	<b>-0.440</b>	<b>-0.198</b>	<b>+0.0208</b>	+0.071	<b>-0.525</b>	<b>-0.293</b>	<b>+0.333</b>
	Error	0.046	0.033	0.0016	0.029	0.038	0.025	0.051
$-21.5 < M_r < -21.0$	$N \geq 10$	-0.995 (37)	0.478 (27)	0.0776 (11)	0.871 (17)	-5.176 (29)	-1.181 (18)	4.925 (40)
$-21.5 < M_r < -21.0$	$4 \leq N \leq 9$	-0.818 (22)	0.546 (15)	0.0697 (7)	0.840 (11)	-4.962 (21)	-1.101 (14)	4.824 (24)
$-21.5 < M_r < -21.0$	$0 \leq N \leq 3$	-0.662 (25)	0.594 (18)	0.0639 (5)	0.806 (9)	-4.813 (20)	-1.029 (14)	4.747 (26)
$-21.5 < M_r < -21.0$	$N$ slope	<b>-0.328</b>	<b>-0.112</b>	<b>+0.0132</b>	<b>+0.065</b>	<b>-0.354</b>	<b>-0.152</b>	<b>+0.173</b>
	Error	0.044	0.032	0.0012	0.019	0.035	0.023	0.046
$-21.0 < M_r < -20.5$	$N \geq 10$	-0.887 (51)	0.478 (37)	0.0686 (14)	0.856 (21)	-5.069 (45)	-1.152 (29)	4.910 (54)
$-21.0 < M_r < -20.5$	$4 \leq N \leq 9$	-0.585 (28)	0.625 (20)	0.0574 (7)	0.839 (13)	-4.758 (23)	-1.010 (15)	4.750 (28)
$-21.0 < M_r < -20.5$	$0 \leq N \leq 3$	-0.429 (33)	0.685 (24)	0.0529 (9)	0.830 (12)	-4.560 (28)	-0.906 (19)	4.688 (31)
$-21.0 < M_r < -20.5$	$N$ slope	<b>-0.427</b>	<b>-0.190</b>	<b>+0.0141</b>	+0.024	<b>-0.482</b>	<b>-0.237</b>	<b>+0.194</b>
	Error	0.059	0.043	0.0016	0.024	0.051	0.033	0.058
$M_g < -21.8$	$0.15 < z < 0.25$	-1.508 (47)	0.228 (34)	0.1066 (15)	0.876 (32)	-5.590 (43)	-1.457 (28)	5.095 (49)
$M_g < -21.8$	$0.25 < z < 0.35$	-1.315 (41)	0.301 (30)	0.1040 (13)	0.833 (27)	-5.332 (56)	-1.277 (37)	5.030 (75)
$M_g < -21.8$	$0.35 < z < 0.45$	-0.864 (56)	0.587 (42)	0.0936 (19)	0.786 (28)	-4.978 (51)	-1.110 (34)	4.940 (77)
$M_g < -21.8$	$0.45 < z < 0.50$	-0.588 (81)	0.644 (60)	0.0817 (23)	0.715 (47)	-4.315 (78)	-0.795 (53)	4.558 (106)
	Slope per $\Delta z = 0.1$	<b>+0.319</b>	<b>+0.158</b>	<b>-0.0080</b>	<b>-0.051</b>	<b>+0.378</b>	<b>+0.201</b>	<b>-0.138</b>
	Error	0.027	0.020	0.0008	0.017	0.025	0.017	0.033
Model: 8 Gyr	[Z/H]=0.0	-1.849	0.074	0.0353	0.981	-6.272	-1.471	5.338
12 Gyr - 8 Gyr	[Z/H]=0.0	-1.183	-0.480	0.0261	0.216	-1.179	-0.562	0.245
8 Gyr	[Z/H]=0.2 - solar	-0.941	-0.296	0.0502	0.125	-0.906	-0.362	0.194

NOTES.—Stacked spectra and models (Vazdekis 1999) are smoothed until the measured velocity dispersion is  $\sigma = 325 \text{ km s}^{-1}$ . The smoothed spectra are then further convolved with a Gaussian to achieve the resolution that a  $\sigma = 275 \text{ km s}^{-1}$  galaxy would have with the Lick/IDS system. However, unlike the official Lick system, we have kept the spectra in their approximately flux-calibrated form. No attempt to correct the indices to zero velocity-dispersion has been made. The focus is on comparison between the different samples. The 1- $\sigma$  error in each measurement is given in parentheses.

The top set compares different luminosities within the MAIN set. The middle sets compare different environments within a given luminosity bin. The final set compares different redshifts within the LRG set. Each set is fit to a linear regression, and the slope and its error are quoted. The slopes versus environment are computed from the best-fit line considering the three bins to be given abscissa values of 0, 0.5, and 1 from least dense to most dense. Boldface numbers indicate 3- $\sigma$  detections of a non-zero slope.

Model spectra from (Vazdekis 1999) are measured in the same fashion. Results for the 8 Gyr, solar metallicity model are quoted. Also quoted are the difference between the 12 Gyr and 8 Gyr model, both at solar metallicity, and the [Z/H] = 0.2 and solar metallicity model, both at 8 Gyr.

TABLE 2

SLICK INDICES ON AVERAGE SPECTRA

Magnitude	Environment/ Redshift	Fe4383 Å	Ca4455 Å	Fe4531 Å	Fe4668 Å	H $\beta$ Å	Mg <sub>2</sub> mag	Mg <i>b</i> Å
$-22.5 < M_r < -22.0$	All	4.158 (25)	1.017 (12)	2.975 (19)	6.377 (31)	1.583 (13)	0.2570 (2)	3.781 (14)
$-22.0 < M_r < -21.5$	All	4.039 (18)	1.005 (8)	2.959 (11)	6.121 (17)	1.575 (9)	0.2441 (2)	3.684 (12)
$-21.5 < M_r < -21.0$	All	3.959 (18)	0.976 (8)	2.918 (11)	5.774 (20)	1.497 (8)	0.2345 (2)	3.543 (12)
$-21.0 < M_r < -20.5$	All	3.798 (25)	0.933 (7)	2.856 (14)	5.372 (17)	1.472 (7)	0.2265 (2)	3.382 (13)
Slope per mag Error		<b>+0.226</b> 0.022	<b>+0.061</b> 0.008	<b>+0.085</b> 0.014	<b>+0.704</b> 0.020	<b>+0.086</b> 0.009	<b>+0.0202</b> 0.0003	<b>+0.270</b> 0.012
$-22.5 < M_r < -22.0$	$N \geq 10$	4.251 (46)	1.099 (22)	3.002 (40)	6.450 (63)	1.512 (26)	0.2685 (7)	4.006 (28)
$-22.5 < M_r < -22.0$	$4 \leq N \leq 9$	4.133 (40)	1.020 (18)	2.985 (31)	6.324 (41)	1.578 (21)	0.2552 (5)	3.770 (22)
$-22.5 < M_r < -22.0$	$0 \leq N \leq 3$	4.062 (70)	0.977 (32)	2.980 (53)	6.311 (99)	1.674 (38)	0.2477 (10)	3.678 (42)
$-22.5 < M_r < -22.0$	<i>N</i> slope Error	+0.198 0.081	<b>+0.128</b> 0.038	+0.024 0.066	+0.171 0.111	<b>-0.156</b> 0.045	<b>+0.0220</b> 0.0012	<b>+0.358</b> 0.049
$-22.0 < M_r < -21.5$	$N \geq 10$	4.119 (35)	1.030 (13)	3.010 (24)	6.284 (46)	1.521 (25)	0.2559 (7)	3.801 (31)
$-22.0 < M_r < -21.5$	$4 \leq N \leq 9$	3.988 (29)	0.981 (11)	2.932 (20)	6.072 (34)	1.537 (13)	0.2441 (2)	3.655 (12)
$-22.0 < M_r < -21.5$	$0 \leq N \leq 3$	3.976 (44)	0.992 (16)	2.898 (30)	5.952 (39)	1.601 (23)	0.2351 (5)	3.529 (21)
$-22.0 < M_r < -21.5$	<i>N</i> slope Error	+0.158 0.056	+0.043 0.021	+0.116 0.039	<b>+0.325</b> 0.061	-0.083 0.034	<b>+0.0202</b> 0.0008	<b>+0.268</b> 0.036
$-21.5 < M_r < -21.0$	$N \geq 10$	4.006 (41)	0.986 (18)	2.932 (26)	5.881 (43)	1.542 (25)	0.2411 (8)	3.619 (32)
$-21.5 < M_r < -21.0$	$4 \leq N \leq 9$	3.937 (37)	0.959 (14)	2.891 (20)	5.761 (34)	1.529 (16)	0.2368 (5)	3.556 (18)
$-21.5 < M_r < -21.0$	$0 \leq N \leq 3$	3.872 (30)	0.956 (15)	2.874 (20)	5.682 (36)	1.493 (12)	0.2313 (4)	3.437 (15)
$-21.5 < M_r < -21.0$	<i>N</i> slope Error	+0.134 0.051	+0.029 0.024	+0.055 0.033	<b>+0.196</b> 0.057	+0.054 0.026	<b>+0.0101</b> 0.0008	<b>+0.199</b> 0.032
$-21.0 < M_r < -20.5$	$N \geq 10$	3.889 (60)	0.957 (28)	2.903 (42)	5.535 (61)	1.519 (27)	0.2348 (11)	3.490 (51)
$-21.0 < M_r < -20.5$	$4 \leq N \leq 9$	3.827 (34)	0.966 (10)	2.879 (25)	5.322 (36)	1.452 (16)	0.2282 (5)	3.420 (22)
$-21.0 < M_r < -20.5$	$0 \leq N \leq 3$	3.719 (41)	0.907 (16)	2.834 (23)	5.335 (43)	1.474 (19)	0.2233 (5)	3.313 (22)
$-21.0 < M_r < -20.5$	<i>N</i> slope Error	+0.179 0.071	+0.073 0.029	+0.074 0.045	+0.160 0.073	+0.030 0.033	<b>+0.0107</b> 0.0011	<b>+0.192</b> 0.048
$M_g < -21.8$	$0.15 < z < 0.25$	4.149 (70)	1.041 (29)	3.016 (49)	6.663 (82)	1.607 (40)	0.2670 (8)	3.934 (34)
$M_g < -21.8$	$0.25 < z < 0.35$	4.157 (78)	1.050 (38)	2.952 (51)	6.334 (81)	1.595 (28)	0.2622 (8)	3.863 (35)
$M_g < -21.8$	$0.35 < z < 0.45$	4.004 (73)	0.991 (32)	2.891 (42)	6.045 (66)	1.713 (22)	0.2423 (11)	3.608 (43)
$M_g < -21.8$	$0.45 < z < 0.50$	3.634 (91)	0.911 (45)	2.802 (77)	5.954 (109)	1.810 (46)	0.2287 (21)	3.418 (86)
Slope per $\Delta z = 0.1$ Error		<b>-0.152</b> 0.036	-0.039 0.016	-0.068 0.026	<b>-0.259</b> 0.040	<b>+0.076</b> 0.018	<b>-0.0123</b> 0.0006	<b>-0.166</b> 0.023
Model: 8 Gyr	[Z/H]=0.0	4.373	...	...	...	1.804	0.2189	3.134
12 Gyr - 8 Gyr	[Z/H]=0.0	0.672	...	...	...	-0.212	0.0314	0.364
8 Gyr	[Z/H]=0.2 - solar	0.777	...	...	...	-0.007	0.0359	0.381

NOTES.—Continuation of Table 2.



TABLE 2

SLICK INDICES ON AVERAGE SPECTRA

Magnitude	Environment/ Redshift	Fe5270 Å	Fe5335 Å	Fe5406 Å	Fe5709 Å	Fe5782 Å	Na D Å	TiO <sub>2</sub> mag
$-22.5 < M_r < -22.0$	All	2.340 (18)	1.873 (19)	1.246 (11)	0.744 (7)	0.594 (8)	3.687 (13)	0.0745 (2)
$-22.0 < M_r < -21.5$	All	2.380 (11)	1.945 (11)	1.273 (6)	0.765 (5)	0.597 (4)	3.493 (7)	0.0723 (2)
$-21.5 < M_r < -21.0$	All	2.348 (10)	1.919 (8)	1.263 (5)	0.771 (5)	0.587 (3)	3.295 (5)	0.0709 (2)
$-21.0 < M_r < -20.5$	All	2.292 (13)	1.856 (14)	1.228 (9)	0.769 (6)	0.573 (4)	3.096 (7)	0.0701 (1)
Slope per mag		<b>+0.050</b>	+0.031	+0.017	−0.014	<b>+0.018</b>	<b>+0.395</b>	<b>+0.0027</b>
Error		0.013	0.014	0.008	0.006	0.005	0.008	0.0001
$-22.5 < M_r < -22.0$	$N \geq 10$	2.361 (25)	1.924 (26)	1.274 (18)	0.755 (15)	0.625 (14)	3.934 (32)	0.0778 (4)
$-22.5 < M_r < -22.0$	$4 \leq N \leq 9$	2.341 (25)	1.911 (27)	1.248 (20)	0.757 (9)	0.600 (13)	3.708 (18)	0.0744 (4)
$-22.5 < M_r < -22.0$	$0 \leq N \leq 3$	2.374 (37)	1.889 (39)	1.261 (34)	0.733 (15)	0.594 (16)	3.583 (24)	0.0729 (8)
$-22.5 < M_r < -22.0$	$N$ slope	−0.005	+0.034	+0.023	+0.022	+0.033	<b>+0.336</b>	<b>+0.0055</b>
	Error	0.043	0.046	0.036	0.022	0.022	0.040	0.0008
$-22.0 < M_r < -21.5$	$N \geq 10$	2.398 (27)	1.950 (28)	1.284 (24)	0.746 (10)	0.588 (11)	3.678 (21)	0.0759 (4)
$-22.0 < M_r < -21.5$	$4 \leq N \leq 9$	2.334 (14)	1.913 (15)	1.244 (12)	0.763 (7)	0.593 (8)	3.449 (11)	0.0723 (2)
$-22.0 < M_r < -21.5$	$0 \leq N \leq 3$	2.323 (19)	1.930 (26)	1.223 (16)	0.761 (10)	0.583 (10)	3.363 (17)	0.0699 (2)
$-22.0 < M_r < -21.5$	$N$ slope	+0.064	+0.017	+0.057	−0.015	+0.006	<b>+0.300</b>	<b>+0.0056</b>
	Error	0.032	0.038	0.028	0.014	0.015	0.027	0.0004
$-21.5 < M_r < -21.0$	$N \geq 10$	2.390 (36)	1.914 (31)	1.269 (21)	0.755 (15)	0.585 (12)	3.373 (16)	0.0728 (4)
$-21.5 < M_r < -21.0$	$4 \leq N \leq 9$	2.315 (15)	1.875 (20)	1.235 (15)	0.760 (9)	0.577 (6)	3.283 (10)	0.0709 (2)
$-21.5 < M_r < -21.0$	$0 \leq N \leq 3$	2.305 (16)	1.869 (18)	1.217 (13)	0.755 (11)	0.567 (6)	3.251 (12)	0.0701 (2)
$-21.5 < M_r < -21.0$	$N$ slope	+0.057	+0.038	+0.048	+0.001	+0.018	<b>+0.114</b>	<b>+0.0026</b>
	Error	0.034	0.035	0.025	0.019	0.013	0.021	0.0005
$-21.0 < M_r < -20.5$	$N \geq 10$	2.318 (46)	1.846 (30)	1.235 (24)	0.751 (20)	0.566 (15)	3.170 (25)	0.0729 (4)
$-21.0 < M_r < -20.5$	$4 \leq N \leq 9$	2.315 (21)	1.859 (22)	1.243 (16)	0.773 (11)	0.569 (9)	3.122 (10)	0.0699 (2)
$-21.0 < M_r < -20.5$	$0 \leq N \leq 3$	2.226 (28)	1.838 (30)	1.225 (17)	0.758 (14)	0.562 (9)	3.046 (14)	0.0694 (4)
$-21.0 < M_r < -20.5$	$N$ slope	+0.117	+0.007	+0.014	−0.001	+0.006	<b>+0.133</b>	<b>+0.0035</b>
	Error	0.051	0.044	0.029	0.025	0.017	0.027	0.0006
$M_g < -21.8$	$0.15 < z < 0.25$	2.386 (31)	1.967 (36)	1.265 (26)	0.739 (24)	0.576 (22)	3.952 (33)	...
$M_g < -21.8$	$0.25 < z < 0.35$	2.353 (30)	1.890 (33)	1.254 (29)	0.709 (22)	0.628 (24)	3.872 (40)	...
$M_g < -21.8$	$0.35 < z < 0.45$	2.325 (46)	1.834 (49)	1.191 (32)	0.627 (25)	0.555 (26)	3.614 (60)	...
$M_g < -21.8$	$0.45 < z < 0.50$	2.127 (105)	1.762 (107)	1.153 (59)	0.764 (94)	0.579 (77)	3.405 (142)	...
	Slope per $\Delta z = 0.1$	−0.048	−0.067	−0.037	−0.044	−0.007	<b>−0.160</b>	...
	Error	0.024	0.026	0.017	0.017	0.016	0.029	...
Model: 8 Gyr	$[Z/H]=0.0$	2.598	1.907	1.295	...	...	...	...
12 Gyr - 8 Gyr	$[Z/H]=0.0$	0.259	0.220	0.157	...	...	...	...
8 Gyr	$[Z/H]=0.2$ - solar	0.335	0.293	0.217	...	...	...	...

NOTES.—Continuation of Table 2.